Fakultät für Physik und Astronomie
Ruprecht-Karls-Universität Heidelberg

Bachelor's Thesis in Physics
submitted by

Lorenz Brachtendorf

born in Bensheim (Germany)

July 2013

Detection of Protons and Carbon Ions with Depth using Al_2O_3:C,Mg-based Fluorescent Nuclear Track Detectors

This Bachelor's Thesis has been carried out by Lorenz Brachtendorf at the
DKFZ Heidelberg
under the supervision of
Prof. Dr. rer. nat. Peter Bachert
and
Prof. Dr. rer. nat. Oliver Jäkel

Kurzfassung

In der Schwerionentherapie sind genaue Kenntnisse über Fluenz, Energie und Partikeltyp notwendig, um eine angemessene Behandlungsplanung zu gewährleisten. Der aktuelle Stand der Verifikation eines speziell auf einen Patienten ausgerichteten Behandlungsplans umfasst Dosismessungen in einem Wasserphantom. Dies bedeutet eine begrenzte Aussagekraft bezüglich der biologischen Wirkung auf den Tumor und das angrenzende gesunde Gewebe. Eine Technologie, die in-vivo Verifikationen erlauben würde, könnte die Behandlungsplanung deutlich verbessern. Biokompatible fluoreszierende Kernspurdetektoren (FNTDs) wurden daher im Rahmen dieser Arbeit als Vorbereitung bezüglich der Detektion von Schwerionen mit zunehmender Eindringtiefe untersucht.
Am Heidelberger Ionenstrahl-Therapiezentrum wurden dafür FNTDs mit Protonen und Kohlenstoff-Ionen in verschieden Tiefen in PMMA bestrahlt. Die Eignung dieser Detektoren für die Detektion von Schwerionen mit der Tiefe konnte gezeigt werden. Die Protonenflächendichte wurde für Eindringtiefen bis zu 11.5 cm in PMMA mit Abweichungen von 3.3% im Durchschnitt und 4.5% im Maximum von den mit FLUKA simulierten Daten bestimmt. Für Kohlenstoffionen wurde eine Partikelflächendichte, die im Mittel um 6.8% von Behandlungsplanungsdaten abwich, gemessen, was auf die Detektion von Fragmenten, höchstwahrscheinlich Bor-Ionen, zurückzuführen ist.
In weiteren Untersuchungen wurden Methoden zur genauen Bestimmung der Winkelverteilung von Protonen in der Tiefe überprüft. Die Verwendung von Tiefenaufnahmen von Teilchenbahnen ermöglicht jedoch immer noch die genauste Bestimmung von Ablenkungswinkeln von Teilchen. Weiterhin wurden erste Schritte bezüglich der Unterscheidung von Teilchenarten in einem Kohlenstoffstrahl gemacht. Dabei konnte bereits festgestellt werden, dass Kohlenstoff-Ionen und leichtere Fragmente, wie Protonen und Helium-Ionen, aufgrund von sehr unterschiedlichen Fluoreszenzsignalen leicht zu unterscheiden sind.

Abstract

In heavy ion therapy, precise knowledge of fluence, energy and particle type is necessary for an adequate treatment planning. The current status of the verification of a patient's individual treatment plan relies mainly on dose measurements in a water phantom which means a limited validity with respect to the biological effect on tissue. A technology which can be used for accurate in-vivo verifications would improve the planning process considerably. Biocompatible fluorescent nuclear track detectors (FNTDs) were therefore investigated in this thesis as a precursor with respect to the detection of heavy charged particles (HCPs) with penetration depth.

For that reason, irradiations of FNTDs with protons and carbon ions in different depths of PMMA were performed at the Heidelberg Ion-Beam Therapy Center (HIT). In these experiments, the detectors have shown their suitability to detect HCPs with depth. Proton densities for penetration depths lower 11.5 cm in PMMA were determined with an average deviation of 3.3% and a maximum deviation of 4.5% from FLUKA simulated data. In a carbon ion beam, densities of carbon ions deviated systematically by 6.8% on average from treatment planning system data for depths lower 12.4 cm, most likely due to the detection of fragments such as boron ions.

In further investigations, methods for the determination of angular distributions of protons were examined showing that stacks of images give the most accurate information on deflection angles of particles. Furthermore, incipient steps regarding the discrimination of different particle types in a carbon ion beam were done showing that carbon ions and lighter fragments such as protons and helium ions can be discriminated very easily using FNTDs.

Contents

1. Introduction

Particle therapy has become an increasingly successful complementation to conventional therapy in cancer treatment in the last decade [1]. It has shown very promising results in the treatment, especially for some particular tumours [2]. Heavy charged particles (HCPs) such as protons and carbon ions show physically and biologically beneficial effects compared to photons due to an inverse depth dose profile and an energy deposition in a well-defined region with a high linear energy transfer (LET). These effects depend on particle type, kinetic energy and the medium the particle traverses. When HCPs penetrate tissue, however, complex mixed particle fields emerge due to nuclear fragmentation as well as the electronic slowing-down process of the particles.
Therefore, to predict the biological dose accurately, particle fluence and energy distribution as well as particle type need to be determined for an adequate treatment of the individual patient. The current status of the verification of a patient's individual treatment plan relies mainly on dose measurements in a water phantom which means a limited validity with respect to the biological effect on tissue. Uncertainties of approximately 20% for the isoeffective dose were estimated for heavy ions due to large variations in the relative biological effectiveness (RBE) [3]. Therefore, in-vivo verifications of treatment plans are highly desirable.

Fluorescent nuclear track detectors (FNTDs), a novel biocompatible detector type, have shown their suitability to accurately determine the fluence of HCPs [4] and are currently investigated in order to gain information on spectroscopic properties such as particle type and energy [5, 6]. Also, the suitability for clinical applications has been examined in terms of in-vivo ion range measurements [7].
In order to continue this research with the objective of investigating their clinical use, this thesis studied the detection of protons and carbon ions with increasing penetration depth measured by FNTDs. For this purpose, a series of FNTDs were irradiated with protons and carbon ions in different depths of polymethyl methacrylate (PMMA) phantoms. Particle densities were determined for protons and carbon ions and, the intensity signal of particle tracks, which is correlated to LET [5], was analysed with depth for both particle types. Further studies focussed on the discrimination of different particle types in a carbon ion beam and the angular distribution of protons.

Physical background knowledge and all relevant quantities will be given in chapter 2. In the following chapter, a more detailed explanation of FNTDs used in the experiments, the radiation facility, the confocal laser scanning microscope which was used for the read-out of the irradiated detectors as well as the software will be presented. In chapter 4, the preparation and execution of the irradiations at the Heidelberg Ion-Beam

Therapy Center and further analysis are explained. In the following chapter, the results of the irradiations and evaluations will be presented. In chapter 6 and 7, the results will be discussed and a conclusion with an outlook suggesting further steps regarding irradiations of particles with depth using FNTDs and possible evaluation methods are given.

2. Background Knowledge

2.1. Interaction of Heavy Charged Particles with Matter

There are several different types of interaction processes of heavy charged particles (HCPs) with matter. Protons and heavier ions are here considered to be HCPs. The perpendicular distance between the asymptote of a particle's trajectory and the target, known as impact parameter b, is crucial for the type of interaction process. Therefore, one can differentiate the different interaction processes in different categories according to the impact parameter b and the atomic radius r_{atom} of the target [8]:

Large impact parameters ($b \gg r_{atom}$): The interaction processes occurring for impact parameters much greater than the radius of the target atom are known as soft collisions involving the incident particle and the whole atomic shell. Two types of scattering processes which can be divided into elastic and inelastic scattering occur. Elastic collisions only cause a polarisation of the atomic shell due to the charge of the incident particle. This leads to a change of the direction of motion and a slight energy transfer to satisfy momentum conservation which can be neglected for heavy charged particles. In case of excitations or ionisations of the outer shell electrons, the traversing particle also changes its direction and loses a small amount of energy (a few eV) in order to excite or ionise an electron (inelastic scattering). The emitted secondary electrons are low in energy and release their energy in the immediate vicinity. The energy loss per collision is very small, but is still responsible for nearly 50% of the energy loss of the incident particles. Therefore, soft collisions lead to a continuous slowing down of the particles.

Medium impact parameters ($b \simeq r_{atom}$): For impact parameters with similar magnitude as the atomic radius, binary collisions of particles and shell electrons can occur leading to much larger energy transfers. These electrons, referred to as δ-electrons, have larger scattering angles and much higher energies compared to electrons emitted by soft collisions. These interaction processes are therefore called hard collisions.

Small impact parameters ($b \ll r_{atom}$): High-energy particles can penetrate the atomic shell of a target atom leading to interactions with the Coulomb field of the nucleus. If they are scattered without losing kinetic energy, the process will be called Coulomb scattering or elastic nuclear scattering. To a great extent, this is responsible for the deflection of HCPs when penetrating a target. The slight energy loss due to recoil processes can be neglected for swift HCPs. For decelerating particles, however, it becomes relevant. Inelastic scattering causes the incident particle to lose some of its

energy which results in the emission of bremsstrahlung. However, inelastic interactions can be neglected for describing the energy loss of HCPs as it is inversely proportional to the square of the particle's mass.

Very small impact parameters ($b \simeq r_{nucleus}$): For impact parameters approximately equal to the radius of the target's nucleus, direct interactions of the projectile and the nucleus can appear leading to deflection of incident particles. In this inelastic process, the energy transfer can cause fragmentation of HCPs or the target [8].

Mass Stopping Power

According to these interactions processes, the average energy loss dE per path length dl and density ρ of the material, the particle traverses, is known as mass stopping power and can be expressed as the sum of the following three independent components:

$$\frac{S}{\rho} = \frac{1}{\rho}\left(\frac{dE}{dl}\right)_{el} + \frac{1}{\rho}\left(\frac{dE}{dl}\right)_{rad} + \frac{1}{\rho}\left(\frac{dE}{dl}\right)_{nuc} \tag{2.1}$$

where

$\frac{1}{\rho}\left(\frac{dE}{dl}\right)_{el} = \frac{S_{el}}{\rho}$ is the mass electronic stopping power due to hard and soft collisions as described above,

$\frac{1}{\rho}\left(\frac{dE}{dl}\right)_{rad} = \frac{S_{rad}}{\rho}$ is the mass radiative stopping power due to emission of bremsstrahlung in the electric fields of atomic nuclei and electrons, and

$\frac{1}{\rho}\left(\frac{dE}{dl}\right)_{nuc} = \frac{S_{nuc}}{\rho}$ is the mass nuclear stopping power due to elastic Coulomb interactions in which recoil energy is imparted to atoms [9].

The electronic stopping power S_{el} is of particular importance for aluminium oxide crystal-based fluorescent nuclear track detectors (FNTDs) which were used in this thesis. It is the main reason for radiochromatic transformations within the crystal which enables one to detect tracks of heavy charged particles. The core of a track is produced by low-energy electrons whereas the outer shape is formed by high-energy electrons. The energy loss due to these interactions can be described using the Bethe formula. In the non-relativistic case, the electronic stopping power S_{el} can be expressed as:

$$S_{el} = \frac{4\pi e^4 Z_p^2 N Z}{m_e v_p^2} ln \frac{2mv_p^2}{I} \tag{2.2}$$

where e is the charge and m_e the mass of a electron, $N \cdot Z$ is the electron density of the target, v_p the particle velocity, Z_p the charge of the particle and I the mean ionisation energy [10]. This relation explains the inverse depth dose profile since the square of the particle's velocity is inversely proportional to the stopping power. This means that the higher the velocity or kinetic energy of a particle the lower is the energy deposition. The

slowing-down process finally leads to a maximum energy deposition (Bragg peak) before the particle stops in the medium.

2.2. Fluence

The particle fluence $\Phi(\mathbf{r})$ in the center $\mathbf{r}$ of a sphere, integrated over time, kinetic energy and solid angle, can be defined as:

$$\Phi(\mathbf{r}) = \frac{dN}{da} \tag{2.3}$$

where dN represents the number of particles passing through a sphere of cross-sectional area da [11]. The convenience of this definition is that all particles traverse the same area da perpendicularly independent of their direction of motion, as illustrated in Fig. 2.1.

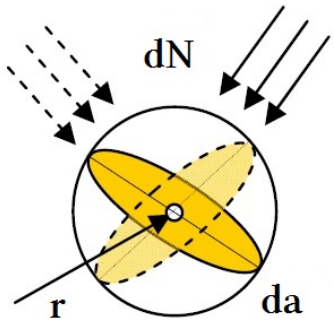

Figure 2.1.: Illustration of the definition of the particle fluence Φ. Reprinted from [12].

For unscattered particles with the total number of particles N penetrating an area $A_\perp$ perpendicularly, the fluence Φ can be simplified to:

$$\Phi = \frac{N}{A_\perp} \tag{2.4}$$

2.3. Linear Energy Transfer

The linear energy transfer (LET) or restricted linear electronic stopping power, L_Δ, is the mean energy loss dE_Δ of a particle along a path length dl due to electronic interactions with the mean sum of the kinetic energies of all released electrons below the threshold Δ:

$$L_\Delta = \frac{dE_\Delta}{dl} \tag{2.5}$$

The unrestricted LET ($L_\Delta \rightarrow \mathrm{L}_\infty$) is therefore equal to the mass electronic stopping power S_{el} [9].

There are two different ways to quantify LET distributions and therefore, there are two different mean values for LET. The frequency distribution of LET, in the following referred to as fluence-weighted LET, is defined in terms of the fluence. The distribution function $F(L) = \Phi_L/\Phi$ gives the fraction of fluence which is associated with LET not exceeding L. Φ is the total fluence and Φ_L is the fluence of particles with LET lower than L. The density of LET in fluence is $f(L) = dF(L)/dL$. The mean fluence-weighted LET can then be defined as:

$$LET_F = \int Lf(L)dL \tag{2.6}$$

The dose-weighted LET is defined in terms of the absorbed dose. Similarly to $F(L)$, the distribution function $D(L)$ is the quotient of the absorbed dose D_L delivered by particles of LET lower than L and the total absorbed dose D. The density of LET in dose is therefore $d(L) = dD(L)/dL$. The mean dose-weighted LET can then be expressed as [11]:

$$LET_D = \int Ld(L)dL \tag{2.7}$$

3. Materials and Methods

3.1. Fluorescent Nuclear Track Detectors

Fluorescent nuclear track detectors (FNTDs) developed by Landauer Inc. (Stillwater, Oklahoma, USA) consist of aluminium oxide single crystals doped with carbon and magnesium (Fig. 3.1). The detectors provided for the experiments of this thesis have a size of $(4 \times 8 \times 0.5)\,\mathrm{mm}^3$. Originally developed for volumetric optical data storage [14], Al_2O_3:C,Mg turned out to be useful for HCP detection due to their high sensitivity for a wide range of LET [15]. Doping the aluminium crystal structure with carbon produces oxygen vacancies making the detector more sensitive for luminescence. These so-called colour centres (F-centres) have a long luminescence lifetime of 35 ms, but additionally doping the crystal with magnesium leads to a much lower lifetime giving F_2^{2+}(2Mg)-centres which makes it much more usable for fast optical imaging. Irradiation of this carbon and magnesium doped crystal with ionising radiation leads to a radiochromatic transformation of the colour centres resulting in fluorescent emission at 750 nm with a lifetime of (80 ± 5)ns when stimulated with 620 nm laser light. The detector can then be read out using confocal microscopy giving a fluorescence signal with its intensity proportional to the energy deposition of the detected particle in the corresponding depth of the crystal [16].

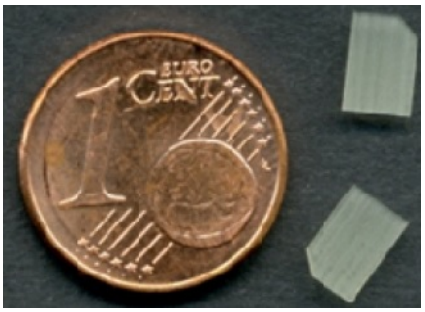

Figure 3.1.: FNTDs with dimensions $(4 \times 6 \times 0.5)\,\mathrm{mm}^3$ compared to a one-cent piece. Reprinted from [13].

3.1.1. Crystal Structure of Al_2O_3:C,Mg

Aluminium oxide, commonly occurring as α-Al_2O_3 (corundum), is a wide gap insulator with a very rigid crystal structure. The hexagonal-close-packed O^{2-} sublattice with Al^{3+} ions, occupying two-thirds of the octahedral lattice sites, is slightly distorted. Each O^{2-} ion is therefore surrounded by four tetrahedral nearest-neighbour Al^{3+} ions. Carbon and magnesium doping leads to the creation of colour centres (F-centres) with most of them containing oxygen vacancy defects having various configurations and charge states. If a vacancy is occupied by two electrons, a neutral F-centre is created and if occupied by one eletron, an F^+-centre is produced which needs an impurity ion such as magnesium for charge compensation. Having two oxygen vacancies next to each other

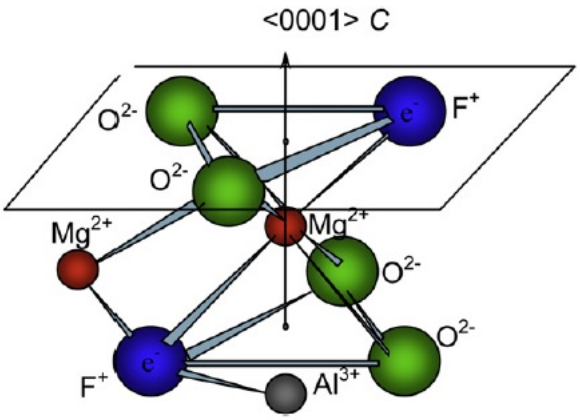

Figure 3.2: Crystall structure of Al_2O_3:C,Mg. Two oxygen vacancies with two magnesium ions for charge compensation form an F_2^{2+}(2Mg). Reprinted from [16].

leads to the formation of two colour centres denoted as F_2-centre. An F_2^{2+}(2Mg)-centre, as seen in Fig. 3.2, therefore refers to two F^+-centres which are charge-compensated by two magnesium ions. This appears to be the main effect for the storage of optical data and is therefore particularly useful for tracking particle trajectories within the crystal volume [17].

3.1.2. Radiochromatic Transformation and Fluorescence

Irradiation of Al_2O_3:C,Mg single crystals with ionising radiation leads to radiochromatic transformations of F_2^{2+}(2Mg)-centres due to electron captures. These colour centres transform as follows:

$$F_2^{2+}(2\mathrm{Mg}) + e^- = F_2^{+}(2\mathrm{Mg}) \tag{3.1}$$

An optical excitation of the these transformed colour centres at around 335 or 620 nm causes an emission of fluorescence photons at 750 nm having a short lifetime of 80 ± 5 ns. In contrast, not transformed F_2^{2+}(2Mg)-centres emit fluorescent light at 520 nm excited by 435 nm laser light with a very short lifetime of 9 ± 3 ns.
This read-out process is non-destructive and the transformed colour centres can only be destroyed by heating the crystal above 700 °C. This means, that the detector can be read out multiple times [16].

3.1.3. Usage as a Fluence and Particle Detector

FNTDs were found to be suitable for a highly accurate fluence determination. The detection efficiency was ascertained to be at least 99.83 % for an LET range from approx. $L_\infty(Al_2O_3) = 0.5$ to 61,000 keV/µm at particle fluences up to $5 \cdot 10^7 \mathrm{cm}^{-2}$ at the minimum [4]. As explained in Sec. 2.2, the particle fluence Φ is defined as the total number of particles N traversing a unit area $A_\perp$ perpendicularly:

$$\Phi = \frac{N}{A_\perp} \tag{3.2}$$

This means for irradiations in the entrance channel with the ion beam perpendicular to the detector surface, that one can assume the number of particles detected per unit area to represent the particle fluence Φ, since changes in direction are insignificantly small for high-energy HCPs and also fragmentation is not an issue in the entrance channel. Therefore, fluences of particle beams can easily be determined with very high accuracy, only restricted by the number of particles on an area, since the number of particles in a particle beam fluctuates, which can be described by the Poisson distribution. The error is therefore given by:

$$\Delta N = \sqrt{N} \Rightarrow \Delta\Phi = \frac{\sqrt{N}}{A_{\perp}} \tag{3.3}$$

Larger areas give therefore smaller relative errors for the number of particles N and the fluence Φ.

In this thesis, FNTDs were not only placed into the entrance channel but also behind PMMA phantoms with different thicknesses. Therefore, the deflection of particles, even for high-energy HCPs as used in the experiments needs to be considered and also, fragmentation processes play a significant role. Therefore, it is quite hard to determine particle fluences. In order to quantify the number of particles in a particular penetration depth the particle density n is introduced:

$$n = \frac{N}{A} \tag{3.4}$$

where N is the number of detected particles per area A.

3.1.4. Usage as a Proxy for Linear Energy Transfer

A correlation of the fluorescence intensity signal of tracks within an irradiated FNTD and LET has been proven recently, depending on the amount of F_2^{2+}(2Mg) colour centres converted to F_2^{+}(2Mg) centres. This dependence on LET was found to be nonlinear. The intensity signal, however, can vary from this correlation which is due to a non-homogeneous distribution of colour centres, but correcting for this difference is easily possible for detectors irradiated with the same particle type and a known LET. The correlation of the intensity and the LET is limited due to the finite number of colour centres in the crystal. However, the detector does not saturate at an $\mathrm{LET}_{\infty}(H_2O) = 8767$ keV/µm [5].
To quantify the intensity signal of tracks, a confocal laser scanning microscope with avalanche photodiodes can be used. A more detailed description concerning the quantification of the fluorescence signal is given in Sec. 3.3.
Furthermore, investigations using STED microscopy have shown that the track width is correlated to the maximum secondary electron range [6].
These properties of the FNTD enable one to use this detector for spectroscopic analysis, i.e. determination of ion type and energy.

3.2. Heidelberg Ion-Beam Therapy Center

The Heidelberg Ion-Beam Therapy Center (HIT) is a clinical radiotherapy facility operated by the Heidelberg University Hospital. Patients have been treated at HIT with protons and carbon ions in three different treatment rooms since 2009 with one room having the world's first carbon ion gantry and the other two providing a fixed horizontal beamline. For research and quality assurance purposes, a fourth room is provided.
Particles are accelerated in a combination of a linear accelerator and a synchrotron before entering one of the treatment rooms. Ion species which can be used at HIT range from protons to oxygen ions with an energy range from 50 to 430 MeV/u obtaining a penetration depth in water from 20 up to 300 mm. Four different beam spot widths are provided in order to irradiate tumours of any shape accurately. Additionally, ten different intensities are available for the beam which can be precisely monitored by the new intensity-controlled raster scan technique. A pencil beam rasters the tumour which is virtually cut in slices with an optimal intensity calculated by the treatment planning software. Thus, a very precise three dimensional irradiation of the tumour with different types of ion beams has been made possible [18, 19].

3.3. LSM 710

For the readout of FNTDs, the inverted confocal laser scanning microscope LSM 710 ConfoCor 3 together with the associated software ZEN 2009 developed by Carl Zeiss Microscopy GmbH was used. The LSM 710 and the ZEN software were provided by the Light Microscope Facility of DKFZ.

For excitation of the radiochromatic transformed colour centres, a helium-neon laser with a wavelength of 633 nm and a nominal power of 5 mW (100 µW at the sample) was utilised yielding near-infrared (NIR) fluorescence from the colour centres of the alumina crystal. Avalanche photodiodes (APDs) were chosen for the detection of fluorescence light as they are highly sensitive to NIR light. To protect the sensitive APDs, overloading can be avoided by reducing the laser power. The photon count rate is limited to 20 MHz with higher rates causing a shut-off of the APDs [20].
In order to select suitable settings for image acquisition, a number of control parameters can be adjusted using the ZEN software. The relative laser power p can be set to values in the range from 0.2% to 100% of the maximum laser power, the possible number of rescans R varies from 1 to 16 scans and the dwell time τ, which is the time the laser stays at one point corresponding to a pixel in the image, varies from 1.3 µs to 177 µs depending on the image size.

For convenient sample handling, FNTDs were placed on glass bottom microwell dishes from MatTek Corp. (Ashland, Massachusetts, USA) with their polished surface facing down towards the laser light. This enables one to easily align the FNTD's position in the microwell dish. The dish was then placed above the objective lens with the optical c-axis

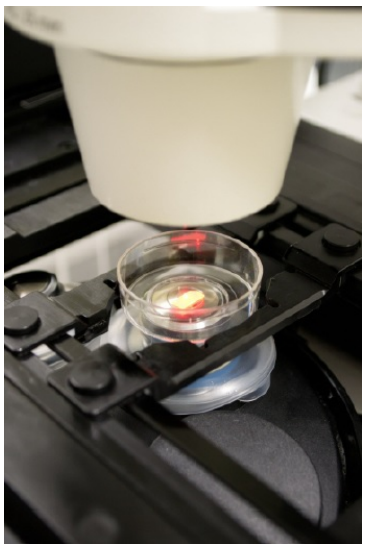

Figure 3.3: A glass bottom microwell dish (MatTek Corp.) with an FNTD inside is placed on the stage of the LSM 710 of the DKFZ. Reprinted from [13]

of the FNTD aligned to the polarisation of the incident laser light. To obtain the best available lateral image resolution (approx. 200nm [20]), the objective lens 63×/1.40NA oil was selected using low-autofluorescent immersion oil.

Acquired images can be stored as LSM files which can be further processed with the ImageJ software or the programming environment R (Sec. 3.4).

In order to compare signals of LSM images with different settings for the dwell time τ and the number of rescans R, the count rate per pixel can be defined as:

$$\eta = \frac{N}{\tau \cdot R} \tag{3.5}$$

where N is the number of counts. The number of photon counts detected by APDs also contains a fluorescence background signal of the FNTD, which needs to be corrected. If the resulting dark count rate η_{DC} and the relative laser power p are taken into account, the 'adjusted count rate' will be as follows:

$$\eta_{adj} = \frac{\eta - \eta_{DC}}{p} \tag{3.6}$$

The adjusted count rate, however, is not the actual count rate, which one would expect. Up to a count rate of 1 MHz, η_{adj} is linearly correlated to the laser power. For higher count rates, the correlation becomes nonlinear until a saturation count rate will be reached. For most calculations in this thesis, the adjusted count rate will suffice [20], since the correlation of LET and count rate with depth was shown qualitatively only.
A more detailed description regarding the read-out of FNTDs using the LSM 710 is given by others [20].

3.4. Software

For image analysis, the Java-based public domain software ImageJ developed by Wayne Rasband [21] and the free software environment for statistical computing R initially designed by Robert Gentleman and Ross Ihaka were applied [22].
For the ImageJ software, the plugin 'Mosaic' developed by the 'MOSAIC' group at the Swiss Federal Institute of Technology Zurich (ETH) was used for particle detection and subtraction of background noise. For a detailed description of the feature point tracking algorithm, the originators' article can be consulted [23]. A good explanation of the corresponding 'Particle Tracker' tool and the histogram-based background subtractor is given by S. Hoof [24].
For further analysis of images, the customised not published R package 'FNTD' was utilised, developed by S. Greilich et al. in the 'Heavy Ion Therapy' group at DKFZ.

Simulations were done using the fully integrated particle physics MonteCarlo simulation package FLUKA developed by Alberto Fass, Alfredo Ferrari, Johannes Rantf, Paolo Sala and others [25, 26].
For the preparation of the irradiations at the Heidelberg Ion-Beam Therapy Center (HIT), treatment planning system (TPS) basic data, also referred to as SPC files, were used. These files are clinically utilised and were provided by HIT.
For further analysis of the SPC files and for calculations of linear energy transfers (LET) of particles, the 'libamtrack' library and the corresponding R package was used [27].

4. Experiments

In this chapter, the irradiations of FNTDs at the Heidelberg Ion-Beam Therapy Center and the following analysis of the detectors will be explained.
First, the planning process of the irradiations with protons and carbon ions is described in Sec. 4.1. The selection and calculation of a number of desired penetration depths in PMMA is explained in this section. The irradiations at HIT and the parameters concerning the selected ion beams are explained in Sec. 4.2. Details with regard to the subsequent image acquisition of the irradiated FNTDs with a confocal laser scanning microscope can be found in Sec. 4.3 and a detailed explanation of different methods used for the particle detection and particle discrimination for both proton and carbon ion irradiations is given in Sec. 4.4.

4.1. Planning of the Irradiations at HIT

The planning of the experiments for this study at HIT was mainly based on treatment planning system (TPS) basic data. In these files, a beam energy of 142.66 MeV for protons and an energy of 270.55 MeV/u for the carbon ion beam were taken as used in the experiments.
Since the major focus of this thesis was the determination of the depth profile of particle densities as well as the particle discrimination with respect to particle type and angular distribution, the most interesting penetration depths regarding the particle spectra were chosen. However, the number of FNTDs provided for this experiment as well as the irradiation time at HIT was limited. Therefore, ten FNTDs for the proton irradiation and twelve FNTDs for the irradiation with carbon ions were used giving ten and twelve different depths, respectively.
For convenience, poly(methyl methacrylate) (PMMA) with a mass density of 1.18 g/cm^3 was chosen as a target material instead of water. In order to obtain the exact depths in PMMA, a water equivalent path length (WEPL) of 1.154 was used for calculations [28]. In Fig. 4.2, the simulated depth profiles of the particle densities of protons as well as of carbon ions and the resulting fragments are shown.

In order to obtain the exact depths in PMMA for the irradiations at HIT, a short section between the beamline and the iso-centre, where the FNTDs were placed, needs to be taken into account. This distance was measured to be 2.89 mm in water [S. Brons, HIT, pers. comm.] which corresponds to 2.50 mm in PMMA using the WEPL above. Putting PMMA inserts between the FNTD and the beamline leads to a small change of this gap. Although being a rather small effect, this was also considered for calculations

in order to obtain an accurate depth in PMMA (see Fig. 4.1 for an illustration of the experimental set-up).
In Tab. 4.1 and 4.2, an overview of the thicknesses of inserts as well as the effective depths in PMMA and water are shown.

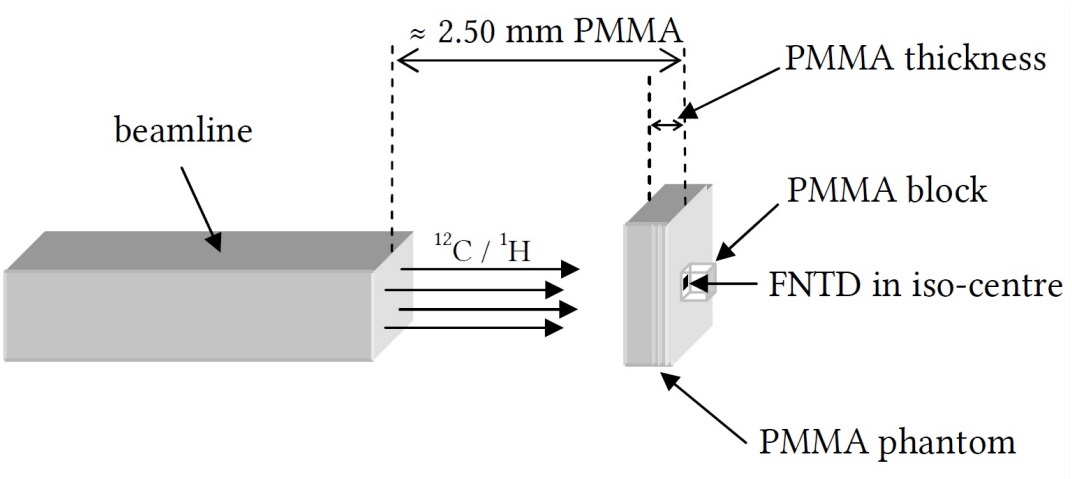

Figure 4.1.: A schematic of the experimental set-up is shown.

FNTD ID	Thickness of the PMMA phantom [cm]	Effective Depth in PMMA [cm]	Effective Depth in H_2O [cm]
lb1000	0	0.250	0.289
lb1001	1.0	1.249	1.444
lb1002	2.9	3.147	3.638
lb1003	4.7	4.946	5.717
lb1004	7.2	7.443	8.605
lb1005	10.9	11.140	12.878
lb1006	11.0	11.240	12.993
lb1007	11.1	11.340	13.109
lb1008	12.2	12.439	14.379
lb1009	14.6	14.837	17.151
lb1010	12.0	12.239	14.148
lb1011	12.1	12.339	14.264

Table 4.1.: Overview of the chosen thicknesses of PMMA slabs for the irradiations with carbon ions. The distance between the beamline and the FNTD as well as the small change of this distance by inserting a PMMA phantom in between were taken into account. The effective depths in PMMA and water are shown additionally.

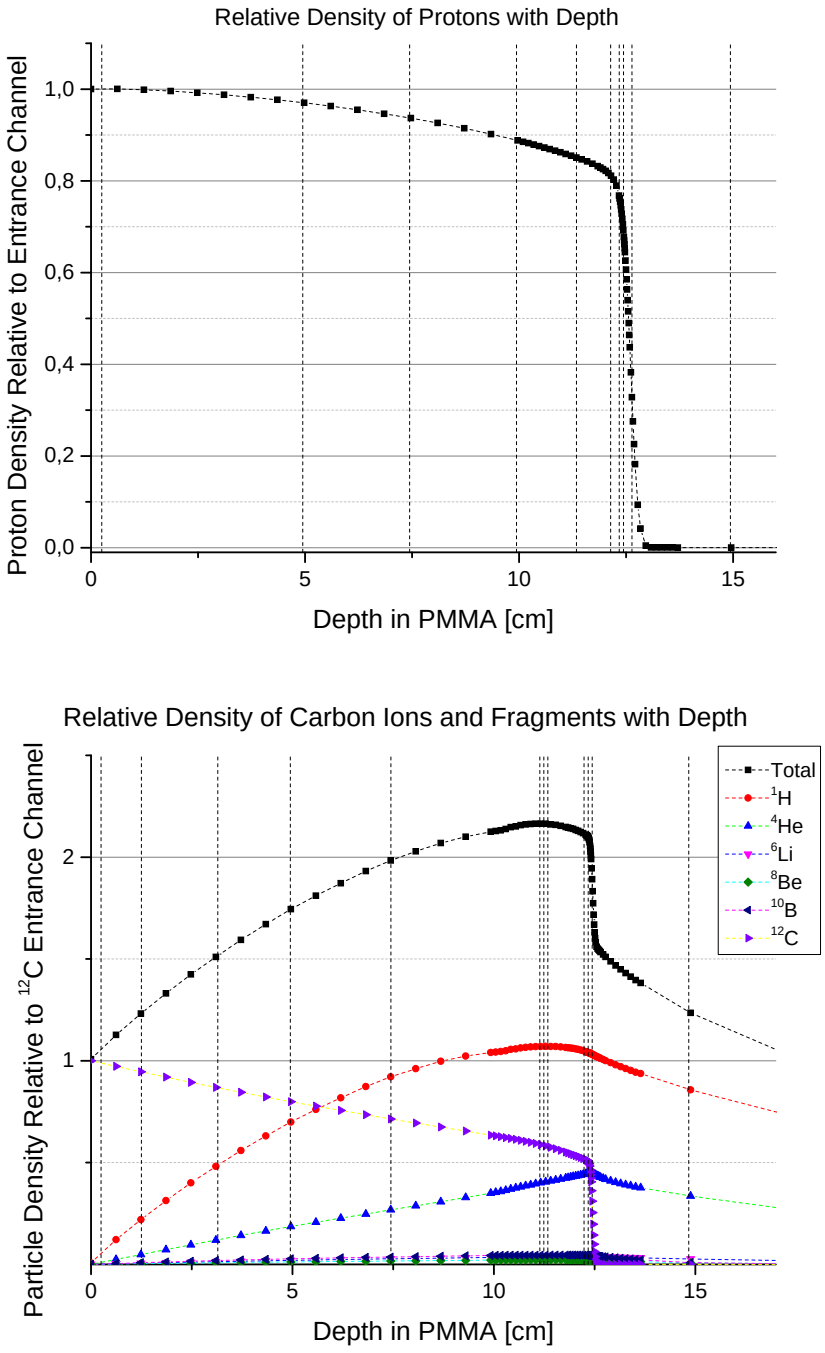

Figure 4.2.: Depth profiles of proton and carbon ion densities, including fragments, are shown using the SPC files. The particle density relative to the entrance channel is plotted as a function of penetration depth in PMMA for both protons and carbon ions. It can be seen that the number of particles increases for a carbon ion beam approx. by a factor of 2.16 due to fragmentation. Especially, protons and helium ions contribute a considerable amount to the particle density. The vertical dashed lines mark the desired penetration depths for the irradiations at HIT.

FNTD ID	Thickness of the PMMA phantom [cm]	Effective Depth in PMMA [cm]	Effective Depth in H_2O [cm]
lb2000	0	0.250	0.289
lb2001	4.7	4.946	5.717
lb2002	7.2	7.443	8.605
lb2003	9.7	9.941	11.492
lb2004	11.1	11.340	13.109
lb2005	11.9	12.139	14.033
lb2006	12.1	12.339	14.264
lb2007	12.2	12.439	14.379
lb2008	12.4	12.639	14.610
lb2009	14.7	14.936	17.267

Table 4.2.: Overview of the chosen thicknesses of PMMA slabs selected for the irradiations with protons. The distance between the beamline and the FNTD as well as the small change of this distance by inserting a PMMA phantom in between were taken into account. The effective depths in PMMA and water are also listed.

4.2. Experimental Set-Up and Irradiations at HIT

The irradiations of the provided FNTDs in different depths of PMMA were performed at the Heidelberg Ion-Beam Therapy Center (HIT).
In the first experiment, a monoenergetic beam of protons with an energy of 142.66 MeV and a particle fluence of $5 \cdot 10^6\,1/\mathrm{cm}^2$ was used. In a second experiment, a monoenergetic beam of carbon ions having an energy of 270.55 MeV/u was selected. The particle fluence was set to a lower value of $3 \cdot 10^6\,1/\mathrm{cm}^2$ as fragmentation causes a significant increase (up to the 2.16 fold of the fluence in the entrance channel, see Fig. 4.2) of the number of particles. These fluences were therefore taken in order to guarantee an optimal analysis concerning the particle detection using the 'Mosaic' particle tracker, since particle fluences greater than a certain threshold (approx. $5 \cdot 10^7\,1/\mathrm{cm}^2$) cannot be determined reliably using this approach [4]. The field size of the beam was chosen to be $(10 \times 10)\,\mathrm{cm}^2$ for both particle types in order to ensure a homogenous irradiation of the FNTDs.

The experimental set-up is shown in Fig. 4.3. The detectors were placed in a little notch of a PMMA block which was exactly fitted to the size of an FNTD. It was then adjusted to be perpendicular to the beamline facing the polished surface of the FNTD the beam source. To utilise the homogeneity of the beam in the isocentre, the PMMA block was accurately positioned by using a marking cross on the surface of the block.

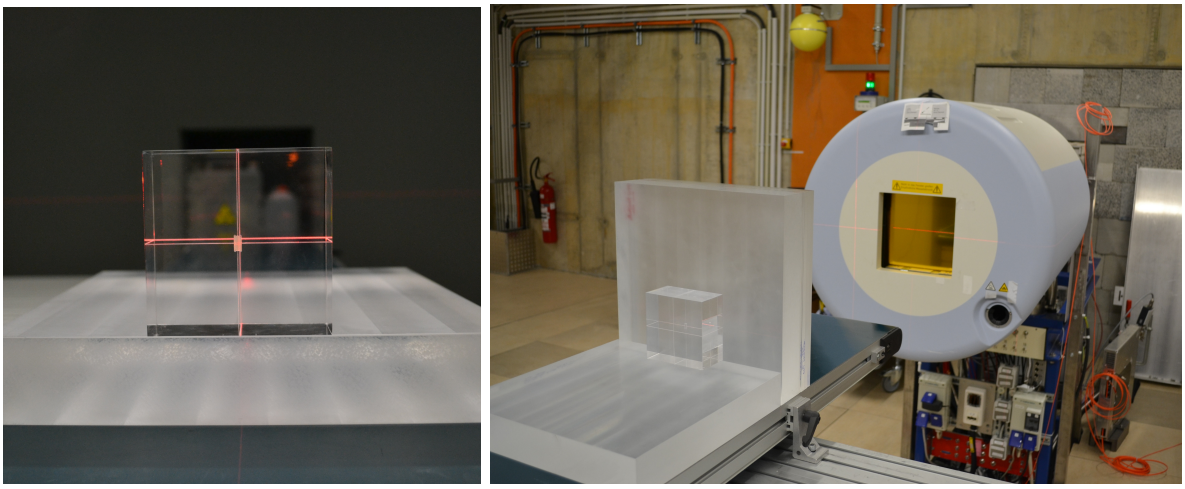

(a) PMMA block (b) Experimental set-up

Figure 4.3.: Image (a): An FNTD is positioned in a small notch of a PMMA block. Image (b): The experimental set-up at HIT with a PMMA phantom in front of the PMMA block with an FNTD inside is shown.

In order to obtain the desired penetration depths, PMMA slabs with thicknesses shown in Tab. 4.1 and 4.2 were placed between the FNTD and the beamline. All PMMA materials were provided by HIT and had different thicknesses from 1 mm up to 5 cm.

4.3. Image Acquisition

The irradiated FNTDs were read out with the LSM 710 (explained in Sec. 3.3). The objective lens 63x / 1.40NA Oil was used in order to obtain the best available resolution for particle detection. The maximum dwell time of 68.92 µs for images of the size (168.69×168.69) µm^2 and a relative laser power of 100% were chosen to achieve a good signal-to-noise ratio (SNR). All images were acquired in an approximate depth of 25 µm below the polished surface of the detector which faced the beam source during irradiation.

For each FNTD irradiated with protons, four images with the above mentioned image size were taken, always at different positions on the detector plane. For each FNTD irradiated with carbon ions, three images of the same size were acquired, also at different positions on the detector surface. These numbers of images were chosen in order to get a Poisson standard deviation lower than 2% for the number of protons and lower than 2.5% for the number of carbon ions at penetration depths in front but close to the Bragg peak using the above mentioned fluences. Also, for all acquired images of FNTDs irradiated with protons four rescans of each position and for images of FNTDs irradiated with carbon ions eight rescans were done in order to obtain a better SNR with the intention to facilitate the detection of particle tracks.
The xy image positions on the plane of the FNTD (the plane perpendicular to the beamline during irradiation) are closely located to the centre of the FNTD surface and

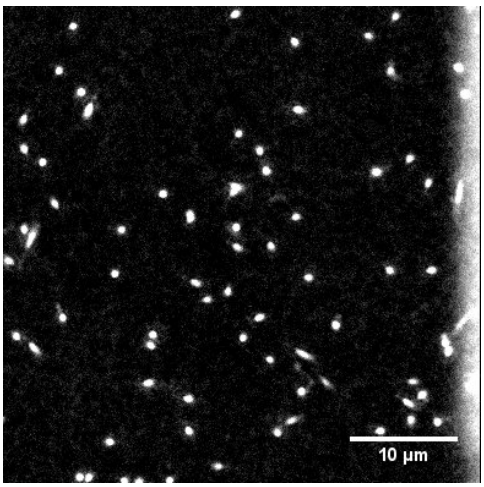

Figure 4.4: Image of the FNTD lb2006: On the right edge of the image, a scanning artefact that occurred during image acquisition can be seen. This artefact was removed by cropping the image to a smaller size.

were carefully chosen to avoid an image acquisition of positions showing dark spots referring to spinel cubical inclusions which exhibit lower fluorescence intensity signals [13]. The detailed positions, together with the complete settings for the read-out process, are noted in Appendix B for each image.

Additionally, in order to investigate angular distributions of particles, as explained in the following sections, z-stacks of images with a depth from 0 to 100 µm and a step size of 1 µm in the detector were acquired for the FNTD lb2007 which was irradiated with protons and for FNTDs lb1008 and lb1011 irradiated with carbon ions. The entire settings for the z-stack image acquisition can also be found in Appendix B.

The selected read-out settings led to a scanning artefact at the right edge of the image (see Fig. 4.4) during image acquisition. This is due to the laser moving to the next line of an image. Therefore, in order to ensure a correct particle detection, all images were cropped to an image size of (164.87×168.69) µm^2 using the ImageJ software.

4.4. Particle Detection and Discrimination

In this section, a couple of different methods for an accurate particle detection and discrimination will be explained. Basis of all methods was the 'Mosaic' plug-in for the ImageJ software.

In a first step, the background was removed using the 'Mosaic' background subtractor. For that, a side length of 20 px was chosen for the sliding window. This value was taken for all analysed images in accordance with investigations on the optimal L parameter [29].
For particle detection, the 'Mosaic' particle tracker was applied. Optimal settings for this process are important and can vary for images of different detectors. However, the radius w as well as the cutoff T_s were the same for all images. The radius was set to 3

px, even when a track's width is larger than this value, as this appeared to be the best value for the detection of two closely adjacent tracks. The cutoff parameter T_s was set to zero in order to detect every potential particle track. The percentile setting, however, had to be adjusted for a couple of images since the fluence decreases with increasing penetration depth and increases for carbon ion beams if fragments are taken into account. The detailed settings are listed in the following sections.

4.4.1. Proton Detection using Manual Discrimination

All acquired images were manually verified for a correct particle detection. Also, a classification in protons having large and low deflection angles was done. Potential particles detected with the 'Mosaic' particle tracker using the settings shown in Tab. 4.3 were differentiated into specific categories, seen in Tab. 4.4.

FNTD ID	Depth in PMMA [cm]	Depth in H_2O [cm]	Percentile r [%]
lb2000	0.250	0.289	0.6
lb2001	4.946	5.717	0.6
lb2002	7.443	8.605	0.6
lb2003	9.941	11.492	0.6
lb2004	11.340	13.109	0.6
lb2005	12.139	14.033	0.6
lb2006	12.339	14.264	0.6
lb2007	12.439	14.379	0.6
lb2008	12.639	14.610	0.4
lb2009	14.936	17.267	-

Table 4.3.: The percentile parameters used for track detection with the 'Mosaic' particle tracker are shown. For all images of each FNTD the same settings were chosen. For images of the FNTD lb1009, the 'Mosaic' particle tracker was not applied, since this FNTD was placed far behind the Bragg peak of 142.66 MeV protons and therefore, no characteristic proton tracks could be identified in images of this detector.

FNTD ID	Depth in PMMA [cm]	Particle Tracker	False Detection	Not Detected	Total	Undeflected	Deflected
lb2000	0.250	5661	121	15	5555	5551	4
lb2001	4.946	5248	123	36	5161	5111	50
lb2002	7.443	4982	154	24	4852	4776	76
lb2003	9.941	4677	75	93	4695	4518	177
lb2004	11.340	4334	47	114	4401	4181	220
lb2005	12.139	4204	21	152	4335	4007	328
lb2006	12.339	3953	12	122	4063	3725	338
lb2007	12.439	3605	12	50	3643	3389	254
lb2008	12.639	1700	12	8	1696	1518	178
lb2009	14.936	-	-	-	0	0	0

Table 4.4.: In each table element, the number of particle tracks detected in four images, each of them having a size of (164.87×168.69) µm^2, is shown according to the specific type. The meaning of these categories is explained on the following page.

In order to explain the manually made classification in different categories, a couple of example images are shown in the following. In Fig. 4.5, three images of the FNTD lb2004 can be seen. In image (a), the trajectory of a secondary electron is illustrated with its Bragg peak at the end of the trajectory leading to a detection due to a fairly high intensity of the track. In panel (b) and (c), tracks which were detected twice due to its elongated shape can be seen whereas tracks of similar shape (but lower intensity) were not detected. Detected secondary electrons as well as multiple detected tracks, leaving one of those tracks detected, however, were classified in the category 'False Detection' of Tab. 4.4 and were discarded for further analysis. The single remaining tracks of the deflected particles in images (b) and (c) were added to the category 'Deflected' due to its elongated shapes. Tracks which were not detected with the particle tracker, but certainly are tracks of protons, were taken into account and are therefore listed in the table column 'Not Detected' and if having an elongated shape, it was additionally classified as 'Deflected'.

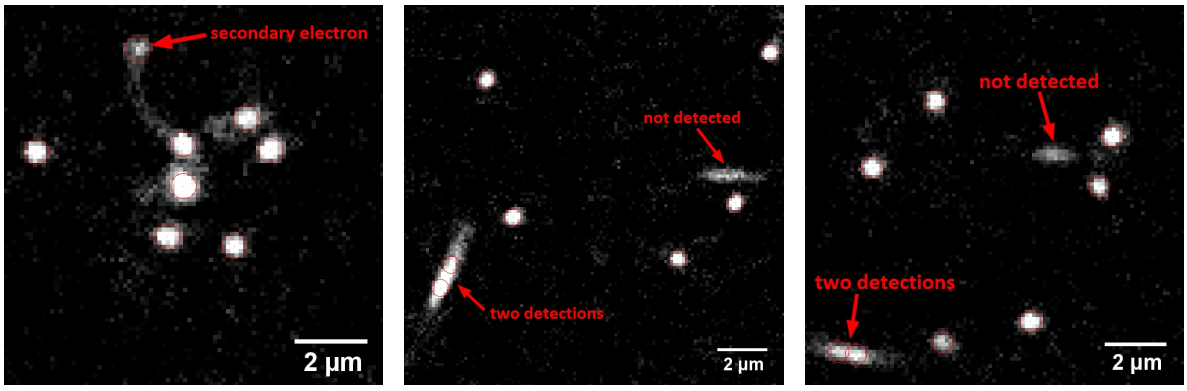

(a) (b) (c)

Figure 4.5.: Images of the FNTD lb2004 irradiated in a depth of 11.340 cm in PMMA. Image (a): The trajectory of a secondary electron with its Bragg peak at the end is misinterpreted as a proton track. Images (b) and (c): Elongated particle tracks with high intensities were detected twice whereas tracks with lower intensities were not detected at all.

To discriminate between particles with large and small deflection angles, a manually determined threshold of elongation is introduced with a track's length greater than this threshold being a 'deflected' particle and lower than this threshold being an 'undeflected' particle. This threshold is set to an approximate elongation of a track, as seen in Fig. 4.7 (a) and (b), showing images acquired of the FNTD lb2006 and lb2007. For this critical threshold, the corresponding deflection angle was determined using a z-stack of images of the FNTD lb2007. In Fig. 4.6, a schematic of the deflection of a particle is shown, illustrating the following relation for the deflection angle θ:

$$\theta = \arctan\left(\frac{\sqrt{(\Delta x)^2 + (\Delta y)^2}}{\Delta z}\right) \tag{4.1}$$

where Δx and Δy are the differences in x and y direction, representing the image plane or the irradiated surface of an FNTD, and Δz specifies the difference in z direction, the direction of the beam during irradiation.

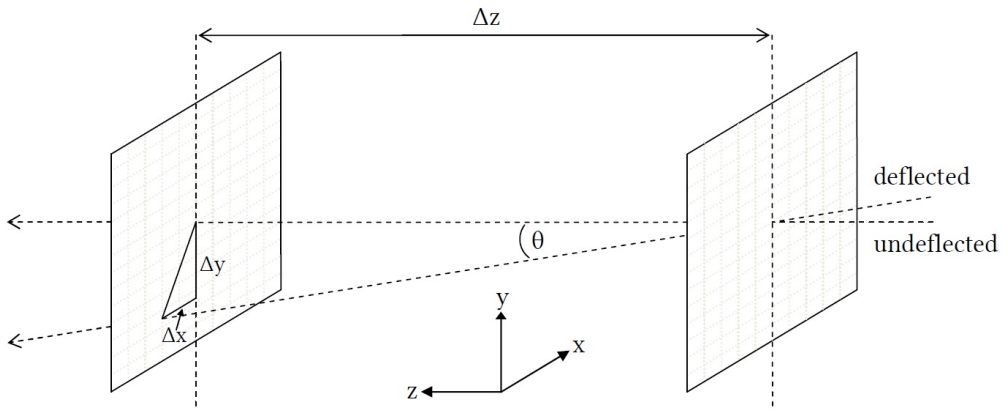

Figure 4.6.: The determination of the deflection angle θ of a particle is illustrated by showing two slices in different depths in z-direction.

For a number of tracks having an elongation which approximately corresponds to the visually defined threshold, the corresponding deflection angles were calculated. Averaging over those values yields a mean deflection angle θ of $18.8° \pm 2.1°$ being the threshold of 'deflected' and 'undeflected' particles.

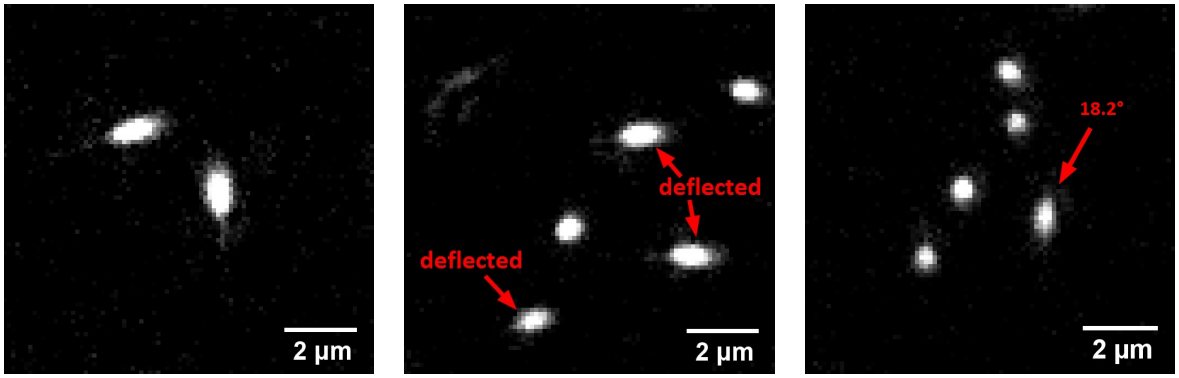

(a) (b) (c)

Figure 4.7.: (a) Image of FNTD lb2006: Both particle tracks represent tracks with the approximate threshold value for the elongation, belonging to 'deflected' particles. (b) Image of FNTD lb2007: Five tracks are shown. Three of them are estimated to indicate deflected particles with the threshold for the track's length and the other two tracks were assumed to be produced by undeflected particles. (c) Z-stack image of FNTD lb2007: A track's length represents roughly the threshold for the elongation. The deflection angle θ of the corresponding particle was calculated to be $(18.2 \pm 0.4)°$.

Additionally, for a couple of tracks with different lengths the corresponding deflection angles were determined in order to gain a better understanding of the visual differences of particles with low and high deflection angles. In Fig. 4.8, two z-stack images of the FNTD lb2007 are shown. For most of the tracks in these images, the deflection angles were calculated, as marked in the image. The angles vary from approx. 1.5° up to 56.0°. Some particles, however, are barely deflected and do not have a clear deflection direction. In panel (a), a track of such a particle can be seen.

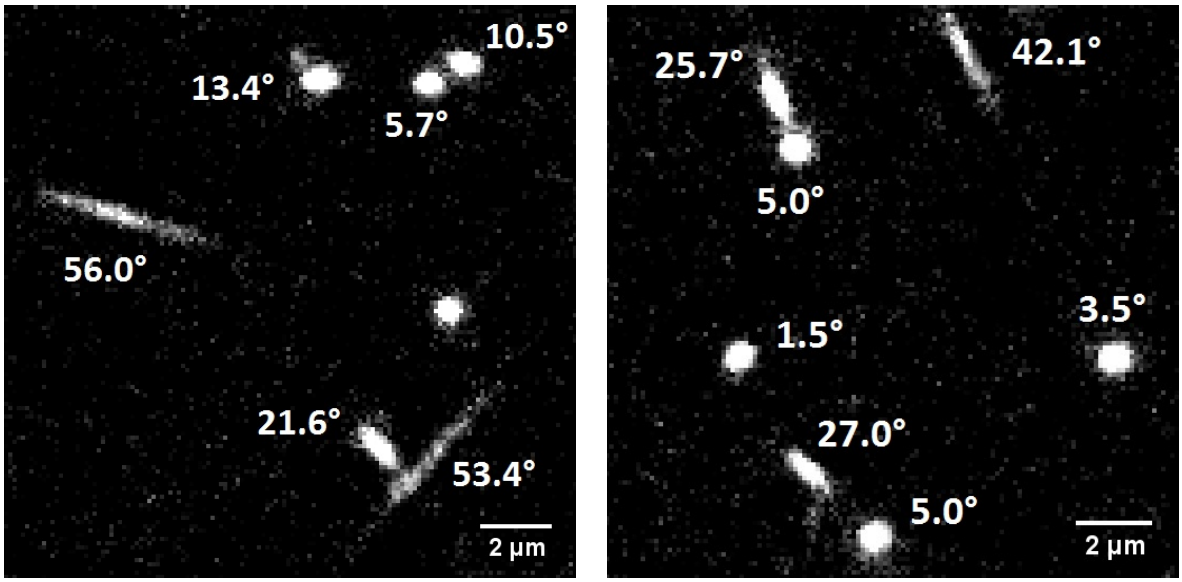

(a) (b)

Figure 4.8.: Z-stack images of the FNTD lb2007: The angles shown in these images illustrate the approximate deflection of the corresponding particle. In the left image, a fairly round particle track can be seen which does not have a clear motion of direction on the xy image plane.

4.4.2. Proton Discrimination using Variance and Covariance Criteria

To investigate the feasibility of angular discrimination of particles using only a single image, statistical measures, more precisely variances and covariances of tracks, were utilised for this method. A correlation of these measures and the deflection angle of a particle as well as the usefulness of these quantities were examined. In order to test this method, a tool of the 'FNTD' package was used to analyse each track on the xy image plane for its intensity-weighted variance and covariance.
Since deflected particles produce elongated tracks on the image plane (see the previous Sec. 4.4.1), the length of a track is to be assessed. Therefore, the relative difference in variances Δs on the xy image plane as well as the covariance $Cov(x, y)$ were determined.

The relative difference in variances was calculated according to the following equation:

$$\Delta s = \frac{Var(x) - Var(y)}{Var(x) + Var(y)} \tag{4.2}$$

The simple variance of a track is not appropriate in this case as the track's width varies with different penetration depths, what would not allow for a reasonable comparison. Furthermore, it needs to be mentioned that the intensity of each pixel was weighted relative to the summed intensity of all pixels of one track. Therefore, the intensity-weighted variance and covariance should be independent of the level of intensity which is necessary in this case since the intensity increases with increasing penetration depth. Hence, variances and covariances of tracks produced by particles in different penetration depths should be comparable.

In order to obtain values for these quantities, the same 'Mosaic' particle tracker settings as in Sec. 4.4.1 were applied. Each detected track was then cut out using a mask radius of 5 px which appeared to be the best value to determine different variances and covariances for tracks of different shapes but was still small enough to avoid cutting out two tracks which are close together. The intensity-weighted variance and covariance were then calculated for each track.
A correlation of an elongated track and a large value for the intensity-weighted covariance as well as for the intensity-weighted relative difference in variances can be identified, as seen in Fig. 4.9. For fairly round tracks, the covariance and the difference in variances are rather small (e.g. see panel (a) in Fig. 4.9). Therefore, separation of tracks with different shapes using this method was investigated.

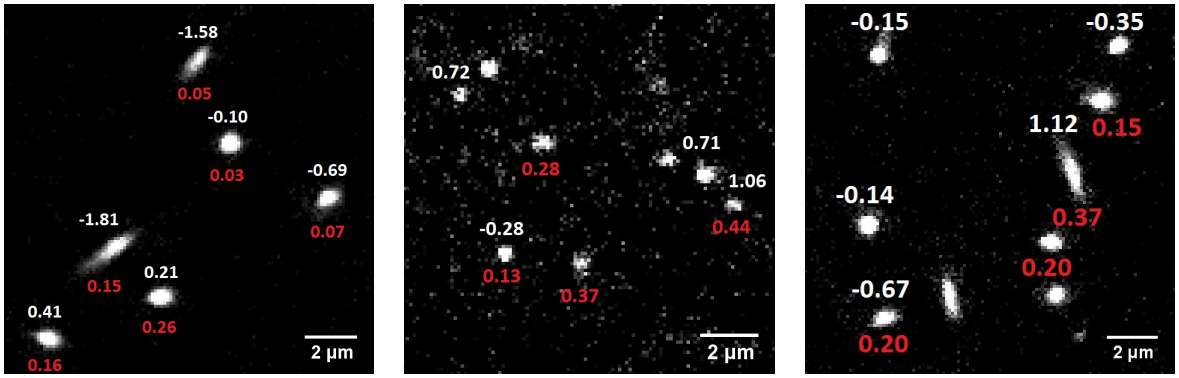

(a) FNTD lb2007 (b) FNTD lb2000 (c) FNTD lb2007

Figure 4.9.: A correlation of Δs or $Cov(x, y)$ and different shapes of tracks can be seen. The values written in red show the absolute values for Δs of the track right above; the covariance is written in white right above the corresponding track. Panel (b): Most tracks do not have a clear shape. (c) Z-stack image: The middle track at the bottom of the image was not detected at all. For all other tracks, the covariances or Δs which are not stated are smaller than 0.11 and 0.09 (in absolute values), respectively.

To find a quantitative correlation of these statistical measures and the deflection angle of a particle, z-stack images of the FNTD lb2007 were utilised. The deflection angle of a particle and the corresponding covariance or relative difference in variances were computed for a number of tracks. However, tracks which are very close to each other were not taken as they can overlap slightly and therefore affect the intensity-weighted variance and covariance of each other significantly. Also, tracks at the edge of the image are cut off and therefore, variances and covariances are distorted and cannot be taken. Except from these two conditions, tracks were chosen randomly giving the plots in Fig. 4.10 and 4.11. The deflection angle is plotted as a function of the relative difference in variances and the covariance, respectively. Assuming a linear correlation, a linear fit was applied to the data, as seen in the plots. Although a linear correlation can be observed, there are also a number of outliers affecting this correlation. The most extreme outliers can be explained by tracks of secondary electrons which are attached to a proton track yielding distorted covariances or variances. Another reason is the fact that $Cov(x, y)$ and Δs do not increase with increasing deflection angle above a certain threshold. This is due to the cutting out of tracks using a disk of limited size. In this case a disk radius of 5 px was chosen.

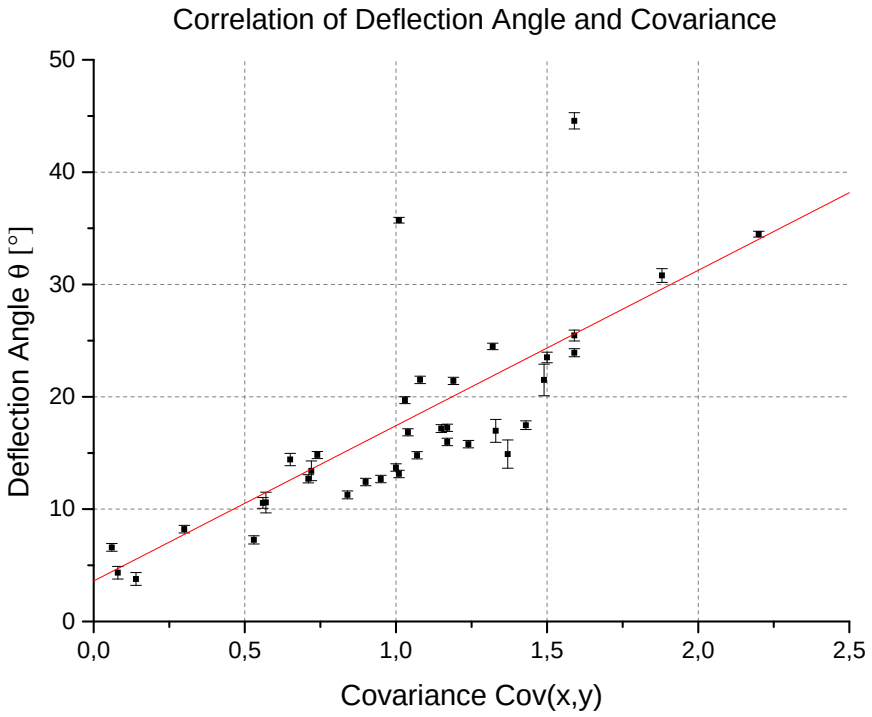

Figure 4.10.: A clear correlation of particles' deflection angles and the intensity-weighted covariances of the corresponding tracks can be identified. A linear fit was used to obtain the covariance for a given deflection angle. Two outliers can be seen. Reasons are explained in the text above. The errors for θ were estimated by slight variations of the track positions in the xy image plane.

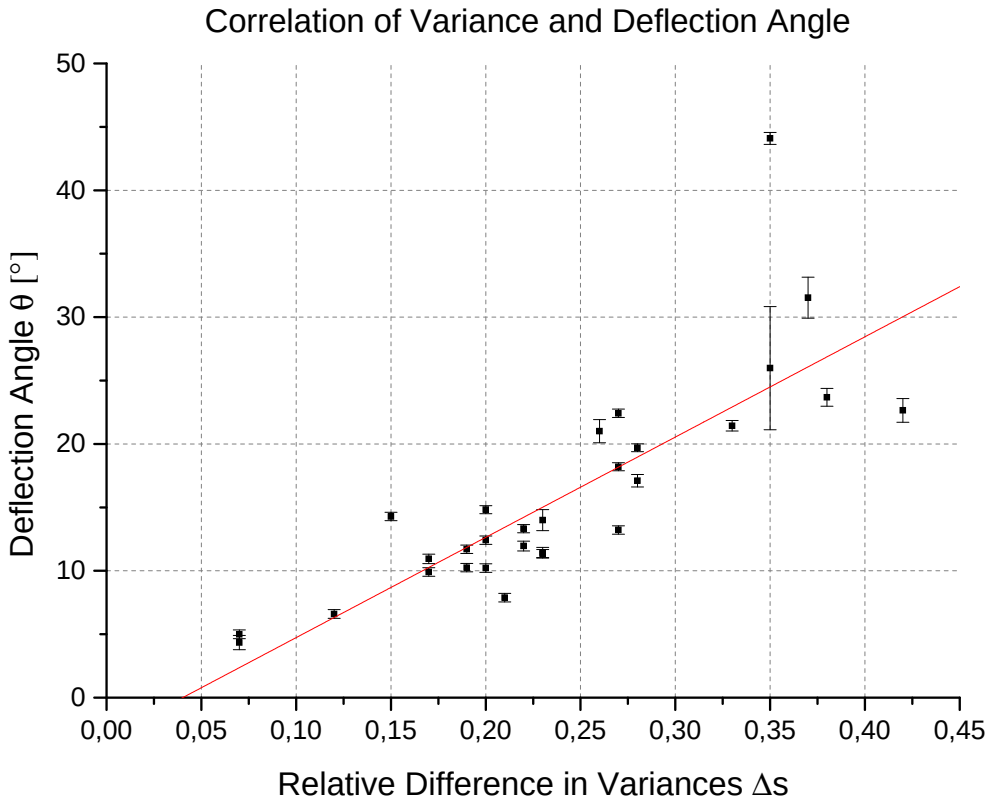

Figure 4.11.: A correlation of deflection angles of particles and the intensity-weighted relative differences in variances Δs of the corresponding tracks can be seen. A linear fit was used to obtain Δs for a given deflection angle θ. Reasons for extreme outliers are explained in the text on the previous page. The errors for θ were obtained by estimating errors for the track positions on the xy image plane.

In order to compare this method with the manual method from the previous section, the same deflection angle ($18.8° \pm 2.1°$) for an angular particle discrimination was chosen. Using the fit parameters from the linear regression, a value of 1.10 ± 0.24 for $Cov(x, y)$ and 0.28 ± 0.06 for Δs were obtained for a given deflection angle θ of 18.8°.
If either a track's value for the covariance or for the relative difference in variances was below these thresholds for $Cov(x, y)$ and Δs, the particle track was considered to be an undeflected proton. Accordingly, for a track with one of its values above these limits, it was regarded to be a deflected particle. The resultant depth profiles of proton densities for both undeflected and deflected particles are shown in Sec. 5.1.2.

In Fig. 4.12, three z-stack images of the FNTD lb2007 with particle tracks showing their values for $Cov(x, y)$ and Δs as well as the deflection angle θ of the corresponding particles are shown.

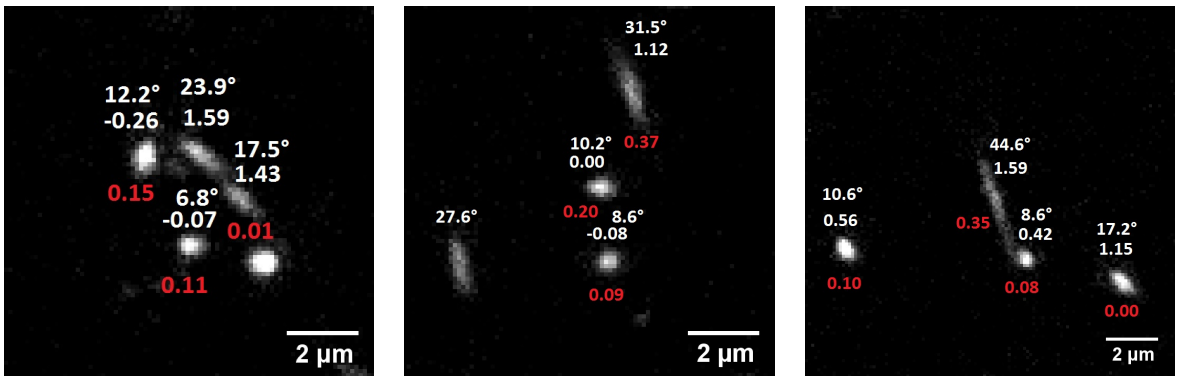

(a) (b) (c)

Figure 4.12.: Z-stack images of FNTD lb2007: Values for the relative difference in variances Δs and the covariance $Cov(x, y)$ as well as the deflection angle θ are shown with the corresponding particle track. The values written in white show $Cov(x, y)$ and θ of the track right below; Δs is written in red right below the track. In panel (a), the wide track downright does not have a clear direction of deflection. After zigzagging on the xy image plane, the track vanishes approx. 35 µm deeper within the crystal. In panel (b), the track on the left-hand side was not detected using the above mentioned settings.

4.4.3. Determination of Fluorescence Intensity Signals of Proton Tracks

In this section, the maximum adjusted count rate η_{adj} (see Sec. 3.3 for the definition) for each track of each penetration depth which meet the criteria in Sec. 4.4.2 were determined. In order to do this, the tool of the 'FNTD' package used in the previous section was utilised again, since it additionally gives the maximum intensity signal of each track which was cut out with a mask radius of 5 px. The adjusted count rate was then determined for each value. Tracks were then distinguished between deflected and undeflected particles according to the variance and covariance criteria from Sec. 4.4.2. For both types, the mean value and the standard deviation for all values of η_{adj} in each penetration depth were calculated.

4.4.4. Monte Carlo Simulation for a Depth Profile of Proton Densities

In order to examine the measurements utilising FNTDs, a Monte Carlo (MC) simulation for protons with a beam energy of 142.66 MeV was performed using the FLUKA simulation package. Therefore, the same penetration depths in PMMA as chosen for the experiments at HIT were taken. For each depth, 200 energy intervals from zero to 200 MeV in steps of 1 MeV and a discrimination of 180 different solid angles from zero to 6.283 sr in steps of 0.03491 sr for 2,000,000 primaries were selected. This was done in order to compare the experimental methods, which investigated the particle density and the angular distribution of protons, with this simulation, which was considered to be the ground truth. Solid angles were converted into polar angles integrating over the azimuthal angle as the whole spectrum of deflections was taken into account for the simulation. The target size was chosen to be of the size of an FNTD as used in the experiments. Since FLUKA determines particle fluences, the corresponding particle densities were computed using the chosen polar angles in order to compare the experimental results with the simulation.

4.4.5. Carbon Ion Detection using the 'Mosaic' Particle Tracker

In order to detect all primary particles without detecting any fragments using the 'Mosaic' particle tracker, the percentile parameters had to be varied considerably.
Since the number of fragments increases with increasing penetration depth, this parameter needs to be low enough to avoid the detection of fragments but has still to be high enough to detect every track produced by carbon ions. As the intensity of tracks varies statistically and also because the track width differs from track to track, there is no well-defined visual difference between heavy fragments and carbon ions. However, for most tracks, it is still possible to discriminate between fragments and primary particles quite well. Therefore, a threshold was visually estimated in each depth. Additionally, the detection process of finding a suitable percentile parameter was tried to be automated. The plots are shown in Appendix C. This method was, however, only used to find the approximate value for the percentile parameter. The final parameters for the percentile r are listed in Tab. 4.5.
In Fig. 4.13, an image of an FNTD irradiated far behind the Bragg peak of 270.55 MeV/u carbon ions is shown. No characteristic carbon ion tracks were identified. In Fig. 4.14, images of FNTDs irradiated in different depths in PMMA can be seen. Tracks of different widths and intensities corresponding to primary particles and fragments as well as many tracks of secondary electrons are visible in these images.
In contrast to the analysis of FNTDs irradiated with protons, the angular distribution was not taken into account for this method as deflection angles were relatively low and therefore, elongated tracks were not an issue for the carbon ion detection using the 'Mosaic' particle tracker.

FNTD ID	Depth in PMMA [cm]	Depth in H_2O [cm]	Percentile r [%]
lb1000	0.250	0.289	0.60
lb1001	1.249	1.444	0.50
lb1002	3.147	3.638	0.40
lb1003	4.946	5.717	0.35
lb1004	7.443	8.605	0.30
lb1005	11.140	12.878	0.25
lb1006	11.240	12.993	0.20
lb1007	11.340	13.109	0.20
lb1008	12.439	14.379	0.08
lb1009	14.837	17.151	-
lb1010	12.239	14.148	0.12
lb1011	12.339	14.264	0.10

Table 4.5.: Percentile settings for the 'Mosaic' particle tracker for all FNTDs irradiated with carbon ions. The same percentile parameters were used for each image of the same detector. The FNTD lb1009 was irradiated far behind the Bragg peak of those carbon ions. Therefore, the particle tracker was not applied for images of this detector.

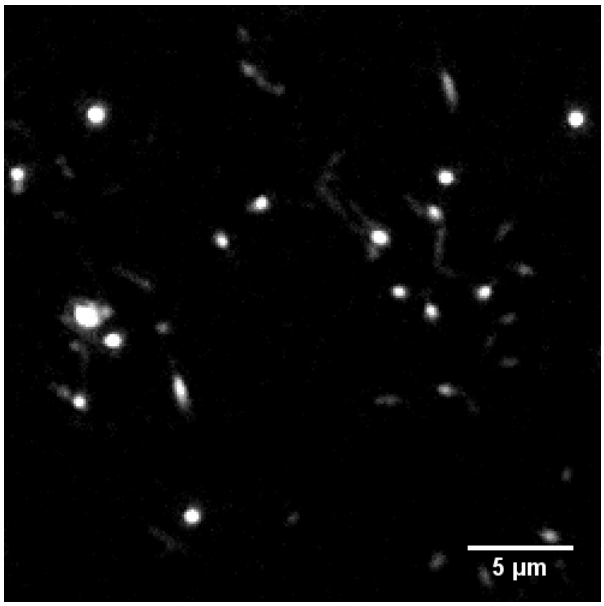

Figure 4.13.: Image of FNTD lb1009: The detector was irradiated far behind the Bragg peak of 270.55 MeV/u carbon ions in a PMMA depth of 14.837 cm. Most tracks correspond to protons or helium ions, but the wide track on the left-hand side was most likely produced by a heavier fragment such as beryllium or boron. According to the SPC files, the probability to detect one carbon ion in this depth is approximately 0.00001.

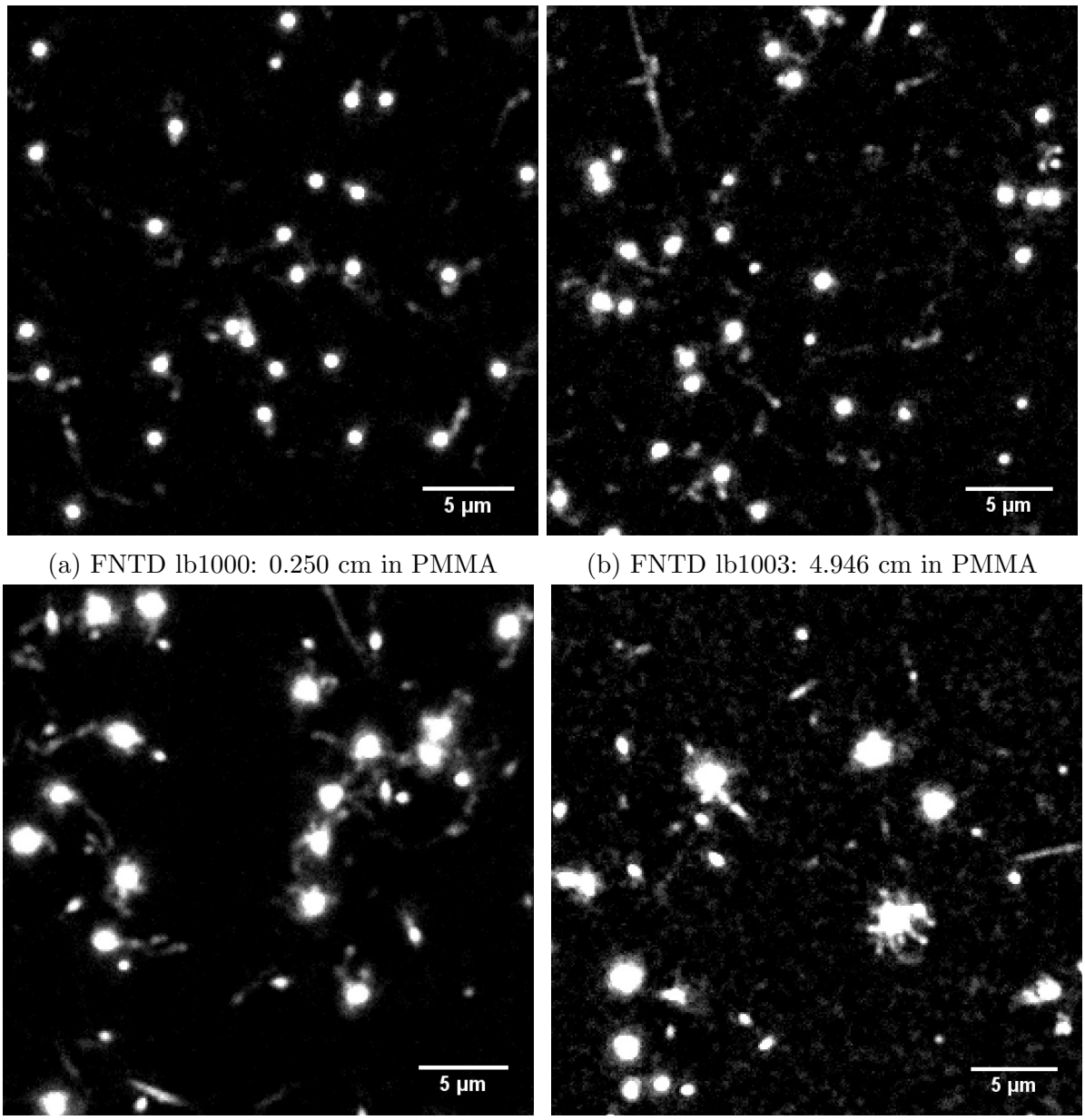

(a) FNTD lb1000: 0.250 cm in PMMA

(b) FNTD lb1003: 4.946 cm in PMMA

(c) FNTD lb1011: 12.339 cm in PMMA

(d) FNTD lb1008: 12.439 cm in PMMA

Figure 4.14.: Images of FNTDs irradiated in different depths of PMMA are shown. The same brightness and contrast settings are used in order to make a visual comparison possible. An increase in the width of carbon ion tracks can clearly be observed. In panel (a), no fragments can be seen whereas in the other images clear tracks of fragments can be identified. Also, elongated tracks produced by fragments with large deflection angles as well as tracks of secondary electrons are visible.

4.4.6. Discrimination of Carbon Ions and Fragments using a Count Rate Criterion and Determination of Fluorescence Intensity Signals

As mentioned in the previous section, the intensities of tracks vary statistically and can be approximated to a Gaussian distribution. This distribution was utilised in order to obtain a depth profile of particle densities of carbon ions.
First, primary particles as well as fragments were detected using the 'Mosaic' particle tracker. Appropriate parameters for the percentile setting are shown in Tab. 4.6. In the following step, all detected tracks were cut out using a mask radius of 5 px. For each track, the maximum intensity was determined and the maximum adjusted count rate η_{adj} was then calculated. Histograms of η_{adj} for each penetration depth are shown in Fig. 5.8 and 5.9 in the next chapter.
In a next step, a double-Gaussian fit was performed for the data of each detector giving mean values and standard deviations for the maximum adjusted count rate of the low-intensity and high-intensity peak (see. Fig. 5.8 and 5.9 for the Gaussian fits).

FNTD ID	Depth in PMMA [cm]	Depth in H_2O [cm]	Percentile r [%]
lb1000	0.250	0.289	0.88
lb1001	1.249	1.444	0.9
lb1002	3.147	3.638	1.0
lb1003	4.946	5.717	1.1
lb1004	7.443	8.605	1.2
lb1005	11.140	12.878	1.3
lb1006	11.240	12.993	1.3
lb1007	11.340	13.109	1.3
lb1008	12.439	14.379	1.1
lb1009	14.837	17.151	0.6
lb1010	12.239	14.148	1.2
lb1011	12.339	14.264	1.1

Table 4.6.: Percentile settings for the 'Mosaic' particle tracker for all FNTDs irradiated with carbon ions. The same percentile parameters were used for each image of the same detector.

5. Results

In this chapter, the results of the experiments performed at the Heidelberg Ion-Beam Therapy Center will be presented.
In Sec. 5.1, the results of the proton discrimination with respect to deflection angles are shown giving a depth profile of the particle density for deflected and undeflected protons for two different methods. Furthermore, the results of the determination of the fluorescence intensity signals of proton tracks as well as a depth profile of the intensities are presented.
In Sec. 5.2, the results of the irradiations with carbon ions are introduced. The depth profiles of the particle density of carbon ions are shown for two different methods and the outcome of the fragmentation detection is given. Furthermore, the results of the determination of fluorescence intensity signals of carbon ion tracks are presented and the corresponding depth profile is shown.
The depth profiles of the particle density for both protons and carbon ions were compared with the FLUKA simulation for protons and with the TPS data for carbon ions. The simulations were assumed to be the ground truth since the results of these measurements using FNTDs have not been validated by other techniques.

5.1. Depth Profiles and Angular Discrimination of Protons

5.1.1. Depth Profiles of Proton Densities using Manual Discrimination

In Tab. 5.1, the manually corrected number of tracks, detected in four acquired images of each detector, is shown. The total number of particles, noted as 'Total', as well as the number of particles having deflection angles lower and greater than $18.8° \pm 2.1°$, noted as 'Undeflected and 'Deflected', respectively, are presented in this table.
It should be mentioned that this manual counting process varies from time to time and depends on the person who discriminates those tracks. This, therefore, gives an unspecified but maybe significant error. However, repeating this approach for a couple of FNTDs, using different contrast and brightness settings for the analysed images, gave variations in the number of 'undeflected' particles and the total amount of particles of less than 2% whereas the number of 'deflected' particles varied clearly stronger.
For these values for the number of protons, the particle densities relative to the particle density in the entrance channel were determined in order to facilitate comparisons with other methods. These relative densities for the different analysed types 'Deflected' and

'Undeflected' particles as well as the 'Total' number of particles are plotted as a function of penetration depth in PMMA, as seen in Fig. 5.1. For comparison, the data of the FLUKA simulation (see Sec. 4.4.4) was added to this plot, given as particle densities relative to the entrance channel.

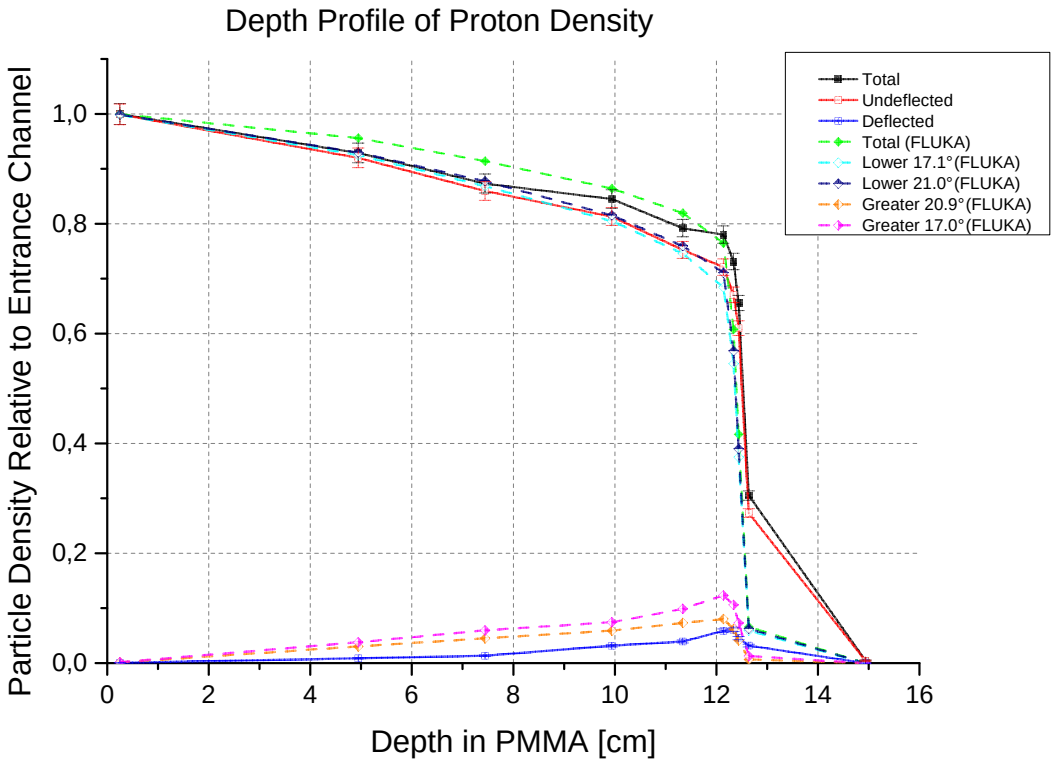

Figure 5.1.: The proton density relative to the entrance channel is plotted as a function of depth in PMMA. The solid lines represent the relative proton density for deflected and undeflected particles having a threshold for the deflection angle of 18.8° using the manual method. Additionally the relative particle density in total is shown. The error bars represent the Poisson standard deviation. The relative proton densities from the FLUKA simulation with a threshold for the deflection angle of approx. 17° and 21° are shown additionally, indicated by dashed lines. A considerable difference in particle densities for deflected protons and therefore, for the particle densities in total can be identified.

FNTD ID	Depth in PMMA [cm]	Depth in H_2O [cm]	Total	Undeflected	Deflected
lb2000	0.250	0.289	$5555 \pm 1.4\%$	$5551 \pm 1.4\%$	$4 \pm 50.0\%$
lb2001	4.946	5.717	$5161 \pm 1.4\%$	$5111 \pm 1.4\%$	$50 \pm 14.2\%$
lb2002	7.443	8.605	$4852 \pm 1.5\%$	$4776 \pm 1.5\%$	$76 \pm 11.5\%$
lb2003	9.941	11.492	$4695 \pm 1.5\%$	$4518 \pm 1.5\%$	$177 \pm 7.6\%$
lb2004	11.340	13.109	$4401 \pm 1.5\%$	$4181 \pm 1.6\%$	$220 \pm 6.8\%$
lb2005	12.139	14.033	$4335 \pm 1.6\%$	$4007 \pm 1.6\%$	$328 \pm 5.6\%$
lb2006	12.339	14.264	$4063 \pm 1.6\%$	$3725 \pm 1.7\%$	$338 \pm 5.5\%$
lb2007	12.439	14.379	$3643 \pm 1.7\%$	$3389 \pm 1.8\%$	$254 \pm 6.3\%$
lb2008	12.639	14.610	$1696 \pm 2.5\%$	$1518 \pm 2.6\%$	$178 \pm 7.5\%$
lb2009	14.936	17.267	0	0	0

Table 5.1.: The number of particles detected in four images of each FNTD (image size 164.87×168.69 μm^2) are classified in different categories. 'Total' denotes the sum of 'Undeflected' and 'Deflected'. The threshold for the deflection angle of 'Deflected' and 'Undeflected' was determined to be $18.8° \pm 2.1°$. The errors represent the Poisson standard deviation and are shown in percent terms.

5.1.2. Depth Profile of Proton Densities and Angular Discrimination using Variance and Covariance Criteria

In Tab. 5.2, the number of particles detected with the 'Mosaic' particle tracker and the number of particles which meet the criteria explained in Sec. 4.4.2 are shown. The category 'Deflected' is to refer to particles which have a deflection angle greater than 18.8°, but it also includes multiple detected tracks of great lengths. Furthermore, a significant number of elongated low-intensity tracks were not detected although representing deflected particles. Therefore, the values in the table column 'Deflected' cannot be considered as an appropriate proxy for deflected particles. In contrast, the column 'Undeflected' shall include every particle with a deflection angle lower than this threshold. For both types, however, the proton densities were determined. The relative proton density was then plotted as a function of penetration depth in PMMA, as seen in Fig. 5.2.

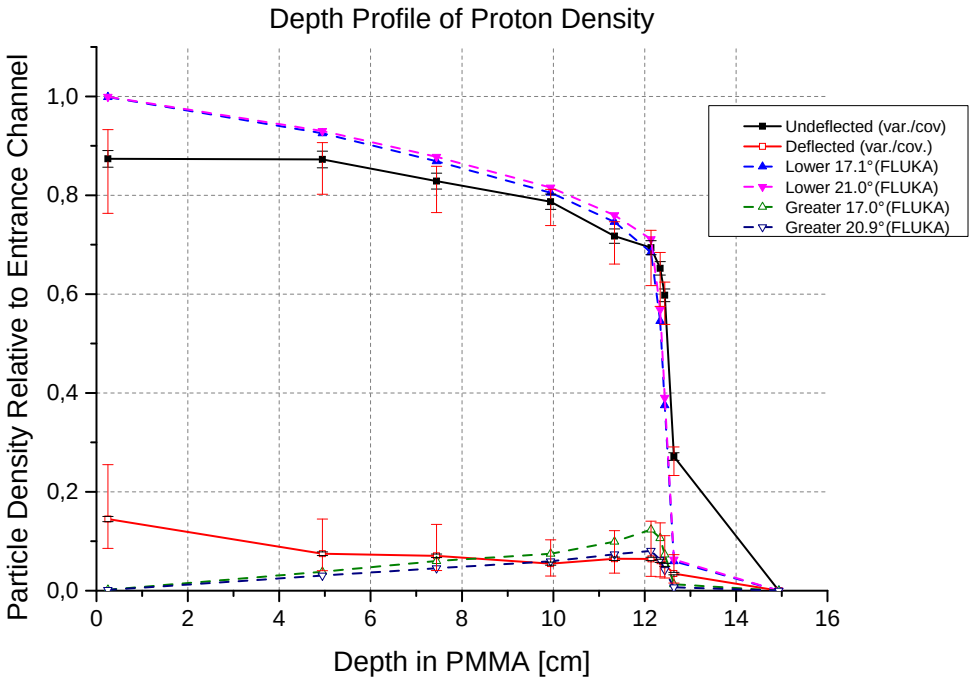

Figure 5.2.: The particle density relative to the proton density in the entrance channel is plotted as a function of depth in PMMA. The reference value for the proton density in the entrance channel was taken from the manual method from Sec. 5.1.1 as it comes most likely near to the truth. The threshold for θ was chosen to be 18.8°. The error bars shown in black represent the Poisson standard deviation. The error bars marked in red result from the errors of the linear regression. The data from the FLUKA simulation is also shown. The proton density relative to the entrance channel is plotted for deflection angles as seen in the legend of the plot.

For comparison, the results of the manual method and the results of the approach using variance and covariance criteria are shown in the same plot in Fig. 5.3.

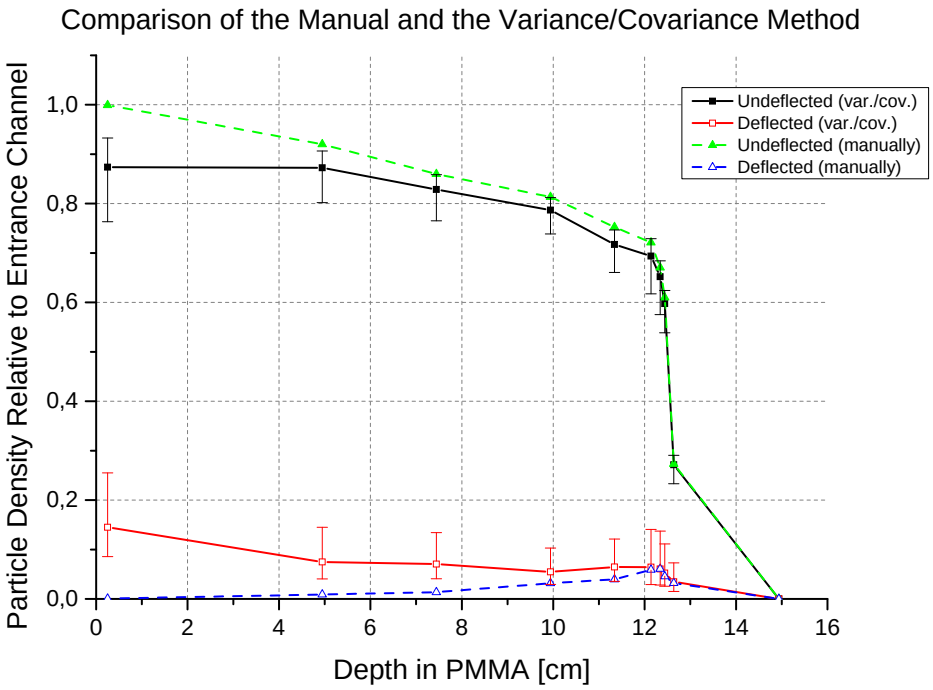

Figure 5.3.: The results of the manual method as well as the method using variance and covariance criteria are shown. The proton density relative to the entrance channel is plotted as a function of depth in PMMA. The reference for the particle density in the entrance channel taken from the manual method was used for both methods since this value is most likely to be close to the truth. The threshold for the deflection angle is 18.8° for both the manual and the variance/covariance method.

FNTD ID	Depth in PMMA [cm]	Depth in H_2O [cm]	Detected Tracks	Undeflected	Deflected
lb2000	0.250	0.289	$5658 \pm 1.4\%$	$4853 \pm 1.5\%$	$805 \pm 3.6\%$
lb2001	4.946	5.717	$5261 \pm 1.4\%$	$4846 \pm 1.5\%$	$415 \pm 4.9\%$
lb2002	7.443	8.605	$4995 \pm 1.5\%$	$4603 \pm 1.5\%$	$392 \pm 5.1\%$
lb2003	9.941	11.492	$4675 \pm 1.5\%$	$4371 \pm 1.6\%$	$304 \pm 5.8\%$
lb2004	11.340	13.109	$4344 \pm 1.6\%$	$3985 \pm 1.6\%$	$359 \pm 5.3\%$
lb2005	12.139	14.033	$4211 \pm 1.6\%$	$3854 \pm 1.7\%$	$357 \pm 5.3\%$
lb2006	12.339	14.264	$3958 \pm 1.6\%$	$3622 \pm 1.7\%$	$336 \pm 5.5\%$
lb2007	12.439	14.379	$3610 \pm 1.7\%$	$3320 \pm 1.8\%$	$290 \pm 5.9\%$
lb2008	12.639	14.610	$1700 \pm 2.5\%$	$1508 \pm 2.6\%$	$192 \pm 7.3\%$
lb2009	14.936	17.267	0	0	0

Table 5.2.: The number of particles, meeting the variance and covariance criteria explained in Sec. 4.4.2, were detected in four images of each FNTD (image size 164.87×168.69 µm^2). The threshold for the deflection angle of deflected and undeflected particles was calculated to be 18.8°. The errors represent the Poisson standard deviation and are shown in percent terms.

5.1.3. Depth Profile of Fluorescence Intensity Signals of Protons

For all detected particles, the maximum intensity within the corresponding tracks were determined and converted into adjusted count rates. In Fig. 5.4 and 5.5, histograms of the maximum adjusted count rate η_{adj} of all detected tracks are shown for each penetration depth. Tracks were discriminated between undeflected and deflected particles according to the criteria from Sec. 5.1.2.

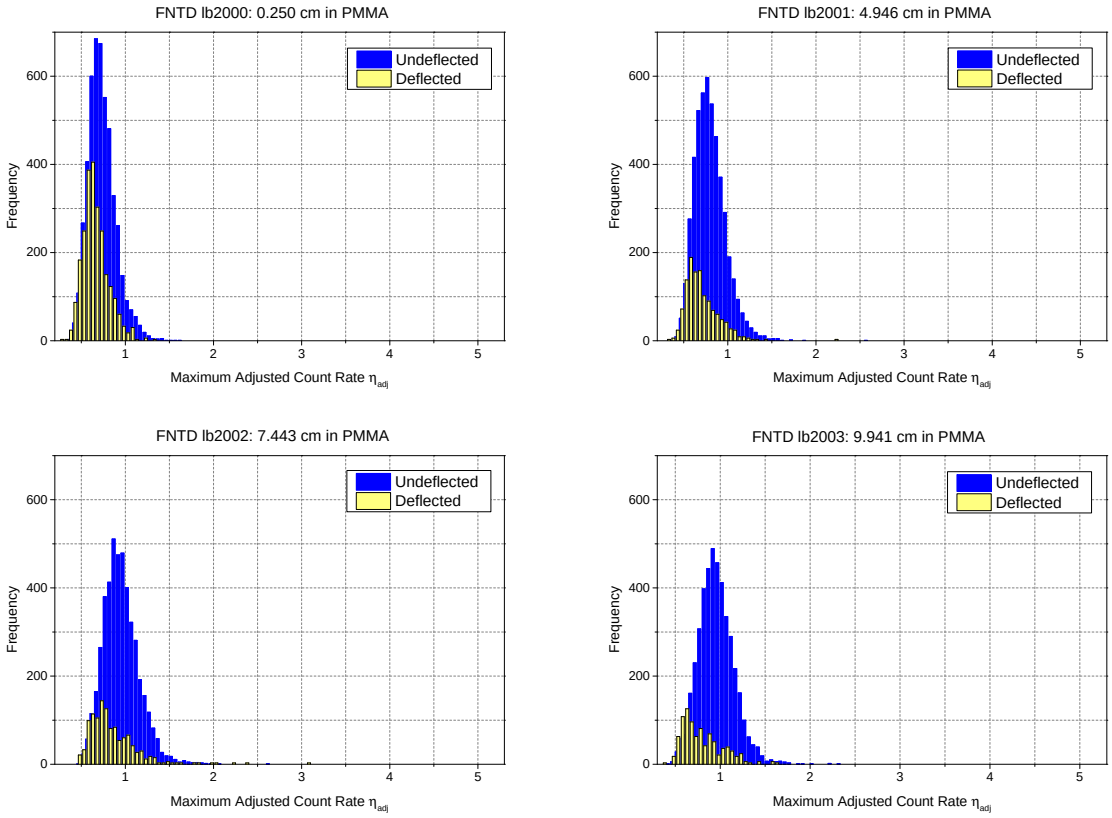

Figure 5.4.: Histograms of the maximum adjusted count rate η_{adj} for FNTDs lb2000 to lb2003. All tracks were discriminated between undeflected and deflected protons. The threshold for the deflection angle is 18.8°. The values for deflected particles were increased threefold to see clearer differences between the count rate of undeflected and deflected particles. The scales for x and y axes are the same for all histograms in order to compare the shift in the count rate, i.e. the fluorescence intensity. Furthermore, a decrease in the number of count rates can be observed.

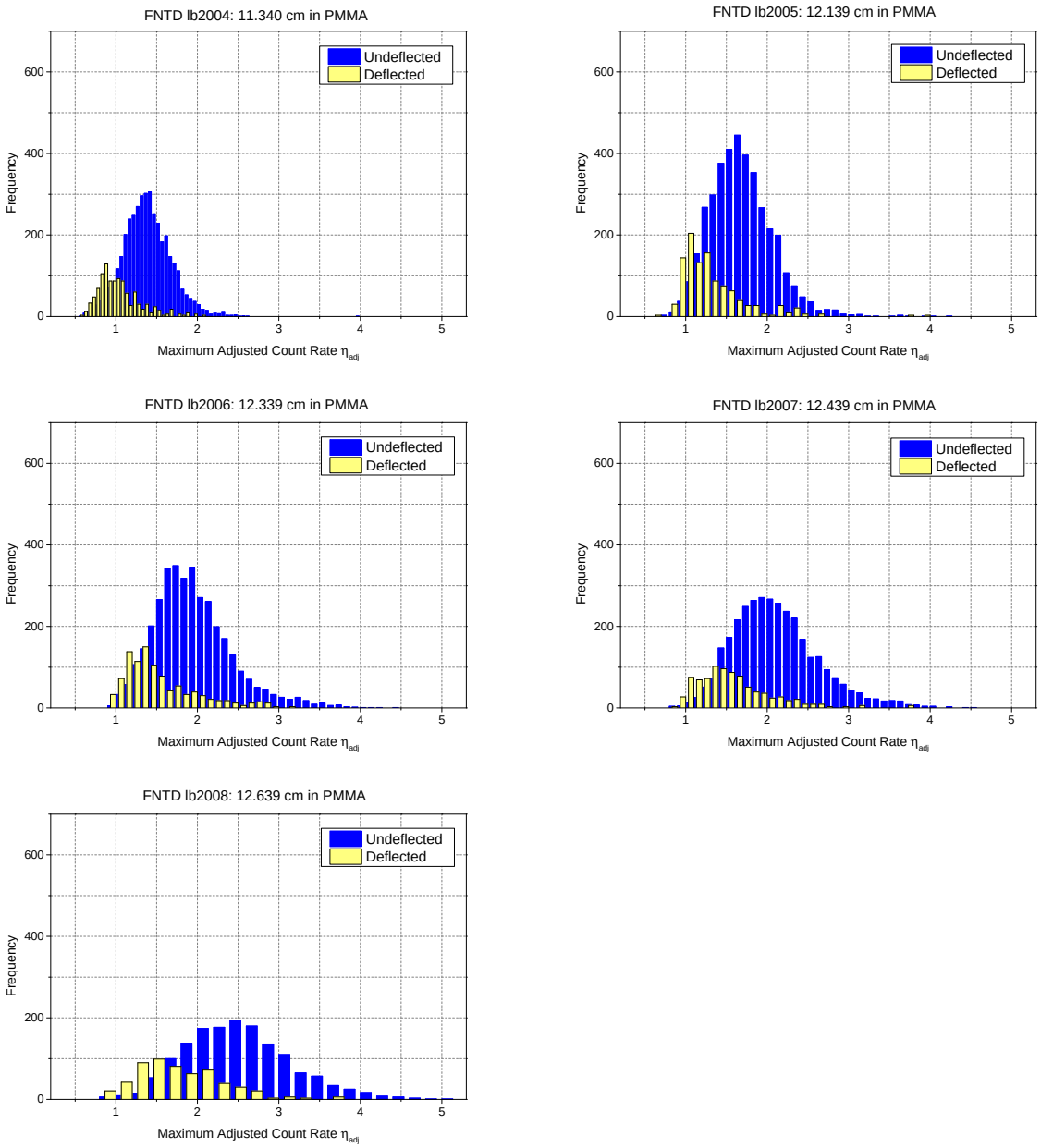

Figure 5.5.: Histograms of the maximum adjusted count rate η_{adj} for FNTDs lb2004 to lb2008. All tracks were discriminated between undeflected and deflected protons (threshold for the deflection angle $\theta = 18.8°$). The values for deflected particles were increased by a factor of 3.

The calculated mean values $\bar{\eta}_{adj}$ of the maximum adjusted count rates are shown in Tab. 5.3 for each penetration depth. These averaged values for the adjusted count rate were then plotted as a function of depth in PMMA for both deflected and undeflected particles, as seen in Fig. 5.6. Also, the dose-weighted and fluence-weighted LET for 142.66 MeV protons is shown with increasing penetration depth in the same plot.

FNTD ID	Depth in PMMA [cm]	$\bar{\eta}_{adj}^{undeflected}$ [MHz] $\pm$ σ [%]	$\bar{\eta}_{adj}^{deflected}$ [MHz] $\pm$ σ [%]
lb2000	0.250	0.742 ± 21.0	0.654 ± 22.3
lb2001	4.946	0.808 ± 22.0	0.702 ± 27.6
lb2002	7.443	0.958 ± 21.2	0.841 ± 34.0
lb2003	9.941	0.964 ± 20.5	0.787 ± 28.2
lb2004	11.340	1.394 ± 21.0	1.033 ± 25.6
lb2005	12.139	1.697 ± 22.7	1.317 ± 30.9
lb2006	12.339	1.956 ± 24.7	1.535 ± 29.3
lb2007	12.439	2.122 ± 24.8	1.579 ± 29.0
lb2008	12.639	2.530 ± 25.7	1.776 ± 30.0
lb2009	14.936	-	-

Table 5.3.: Mean values for the maximum adjusted count rate $\bar{\eta}_{adj}$ with their standard deviations σ are shown for each FNTD.

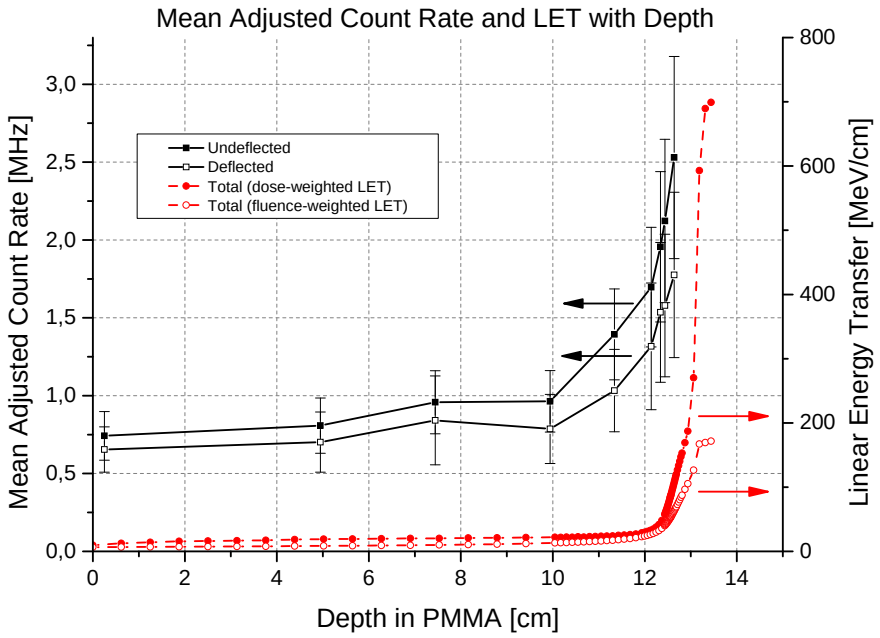

Figure 5.6.: The mean value of the maximum adjusted count rate $\bar{\eta}_{adj}$ is plotted as a function of penetration depth in PMMA for tracks of both undeflected and deflected particles indicated by solid lines. The error bars represent the standard deviation of $\bar{\eta}_{adj}$. The two dashed lines show the dose-weighted and fluence-weighted LET of protons. The data was obtained from the SPC file which was used for the irradiation planning. LETs were calculated using the 'libamtrack' library. It can be seen that the values for deflected particles were systematically underestimated.

5.2. Depth Profiles and Particle Discrimination in a Carbon Ion Beam

5.2.1. Depth Profile of Carbon Ion Densities using the 'Mosaic' Particle Tracker

For the detection of tracks produced by carbon ions the 'Mosaic' particle tracker was used. Appropriate settings for the detection were chosen, as seen in Sec. 4.4.5. However, the visual difference between fragments and carbon ions in the acquired images was not clearly defined.
The number of carbon ions detected in three images with an image size of (164.87 × 168.69) µm^2 is shown in Tab. 5.4. In Fig. 5.7, the density of carbon ions relative to the particle density in the entrance channel was plotted as a function of penetration depth in PMMA. Additionally, the relative density of carbon ions obtained from the SPC file for 270.55 MeV/u carbon ions, which was used for the planning of the experiments, is shown in the same plot.

FNTD ID	Depth in PMMA [cm]	Depth in H_2O [cm]	Number of ^{12}C Ions
lb1000	0.250	0.289	$2472 \pm 2.0\%$
lb1001	1.249	1.444	$2446 \pm 2.0\%$
lb1002	3.147	3.638	$2186 \pm 2.2\%$
lb1003	4.946	5.717	$2073 \pm 2.2\%$
lb1004	7.443	8.605	$1889 \pm 2.3\%$
lb1005	11.140	12.878	$1695 \pm 2.5\%$
lb1006	11.240	12.993	$1592 \pm 2.5\%$
lb1007	11.340	13.109	$1607 \pm 2.5\%$
lb1010	12.239	14.148	$1227 \pm 2.9\%$
lb1011	12.339	14.264	$1203 \pm 2.9\%$
lb1008	12.439	14.379	$757 \pm 3.7\%$
lb1009	14.837	17.151	0

Table 5.4.: The number of carbon ions detected in three images with an image size of (164.87 × 168.69) µm^2 is shown for each depth. The errors represent the Poisson standard deviation and are shown in percent terms. The detector lb1009 was placed in PMMA far behind the Bragg peak of 270.55 MeV/u carbon ions. Therefore, no carbon ions were detected.

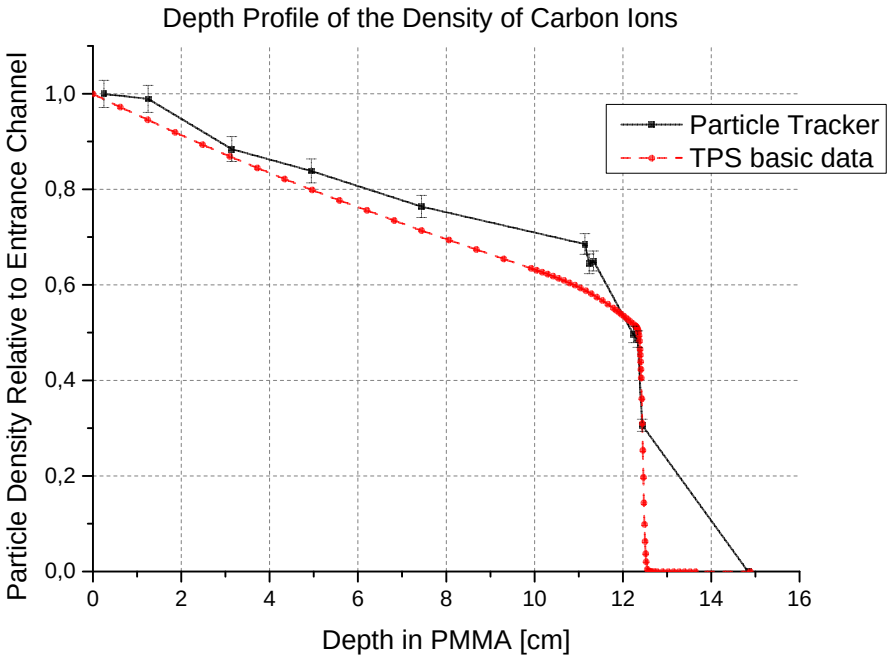

Figure 5.7.: The density of carbon ions relative to the density in the entrance channel is shown as a function of depth in PMMA. The error bars represent the Poisson standard deviation. The relative densities of carbon ions taken from the TPS basic data are also shown. One can see that the experimental results are systematically above the values of the TPS data.

5.2.2. Depth Profile of Carbon Ion Densities using Track Intensity Signals and Depth Profile of Track Intensities

In Fig. 5.8 and 5.9, histograms of the maximum adjusted count rates η_{adj} of all detected tracks are shown for each penetration depth. A double Gaussian fit was used to obtain the mean adjusted count rates for both peaks as well as their standard deviations. The mean values for the count rates of the right peaks are listed in Tab. 5.5. The left peak was, however, not analysed quantitatively due to too many deficiencies in the particle detection using the 'Mosaic' particle tracker, but the data will be discussed in the following section.

In order to obtain the number of tracks produced by carbon ions, each track within a 3σ range on the left-hand side of the peak was considered to be a carbon ion track. For the tail on the right-hand side, all tracks were considered to be carbon ions, even for count rates beyond a 3σ range, since such high count rates are due to overlapping of carbon ion tracks producing much higher count rates. In addition, no fragments which produce such high fluorescence signals emerge in a carbon ion beam. The number of carbon ions detected using this method is shown in Tab. 5.6.

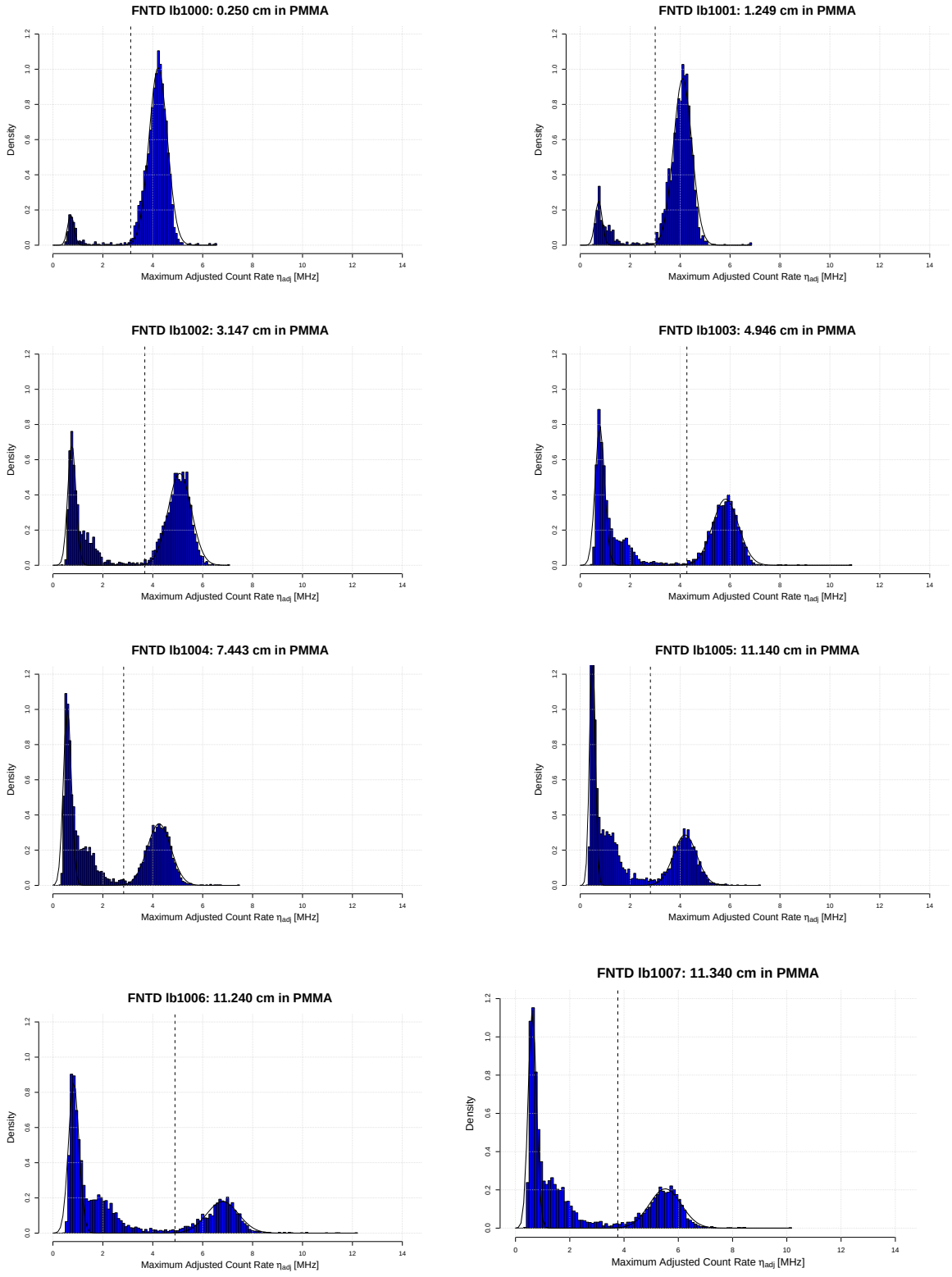

Figure 5.8.: Histograms of the maximum adjusted count rate η_{adj} for FNTDs lb1000 to lb1007. The scale for the x-axis is the same for all histograms in order to compare the shift in the count rate, i.e. the fluorescence intensity. The dashed line represents the 3σ range on the left-hand side of the ^{12}C peak.

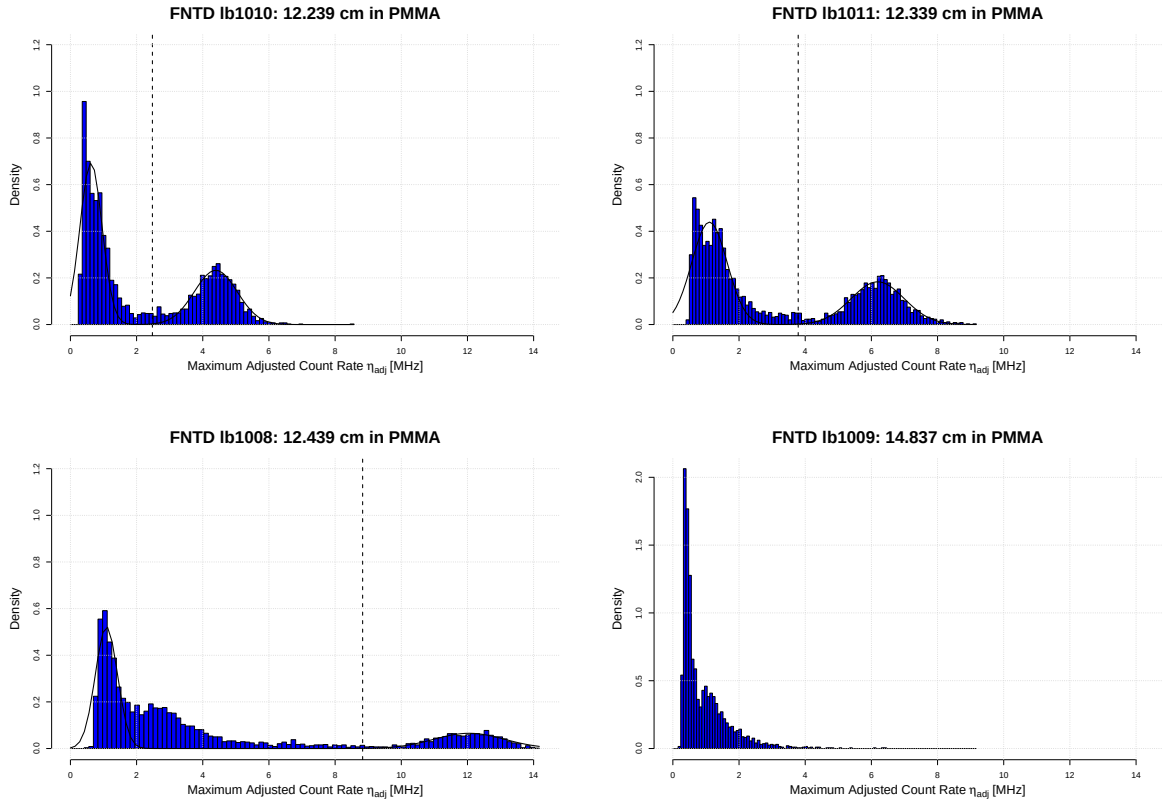

Figure 5.9.: Histograms of the maximum adjusted count rate η_{adj} for FNTDs lb1008 to lb1011 are shown. For the detector lb1009, no peak on the right-hand side of the histogram can be seen. The vertical dashed line represents the 3σ range on the left-hand side of the carbon ion peak. The low-intensity peak was not analysed quantitatively, but qualitative results are discussed in the next chapter.

FNTD ID	Depth in PMMA [cm]	Depth in H_2O [cm]	$\bar{\eta}_{adj}$ [MHz] $\pm\sigma$
lb1000	0.250	0.289	$4.21 \pm 8.7\%$
lb1001	1.249	1.444	$4.10 \pm 8.9\%$
lb1002	3.147	3.638	$5.06 \pm 9.1\%$
lb1003	4.946	5.717	$5.81 \pm 8.9\%$
lb1004	7.443	8.605	$4.25 \pm 11.1\%$
lb1005	11.140	12.878	$4.20 \pm 11.0\%$
lb1006	11.240	12.993	$6.80 \pm 9.4\%$
lb1007	11.340	13.109	$5.52 \pm 10.6\%$
lb1010	12.239	14.148	$4.39 \pm 14.6\%$
lb1011	12.339	14.264	$6.17 \pm 12.9\%$
lb1008	12.439	14.379	$12.01 \pm 8.9\%$
lb1009	14.837	17.151	0

Table 5.5.: Mean values for the maximum adjusted count rate $\bar{\eta}_{adj}$ with their standard deviation σ are shown for each FNTD.

FNTD ID	Depth in PMMA [cm]	Depth in H_2O [cm]	Number of ^{12}C Ions
lb1000	0.250	0.289	$2446 \pm 2.1\%$
lb1001	1.249	1.444	$2417 \pm 2.1\%$
lb1002	3.147	3.638	$2142 \pm 2.2\%$
lb1003	4.946	5.717	$2023 \pm 2.3\%$
lb1004	7.443	8.605	$1828 \pm 2.4\%$
lb1005	11.140	12.878	$1624 \pm 2.5\%$
lb1006	11.240	12.993	$1538 \pm 2.6\%$
lb1007	11.340	13.109	$1571 \pm 2.6\%$
lb1010	12.239	14.148	$1378 \pm 2.7\%$
lb1011	12.339	14.264	$1315 \pm 2.8\%$
lb1008	12.439	14.379	$716 \pm 3.8\%$
lb1009	14.837	17.151	0

Table 5.6.: The number of carbon ions detected in three images with an image size of (164.87×168.69) µm^2 is shown for each depth. The errors represent the Poisson standard deviation and are shown in percent terms. The detector lb1009 was placed in PMMA far behind the Bragg peak of 270.55 MeV/u carbon ions. Therefore, no carbon ions were detected.

In Fig. 5.10, the particle density of carbon ions is plotted as a function of depth in PMMA. Additionally, the data from the SPC file is shown in order to examine the accuracy of this method. Furthermore, the two different methods using the 'Mosaic' particle tracker only and using the count rate criterion are compared in Fig. 5.11.

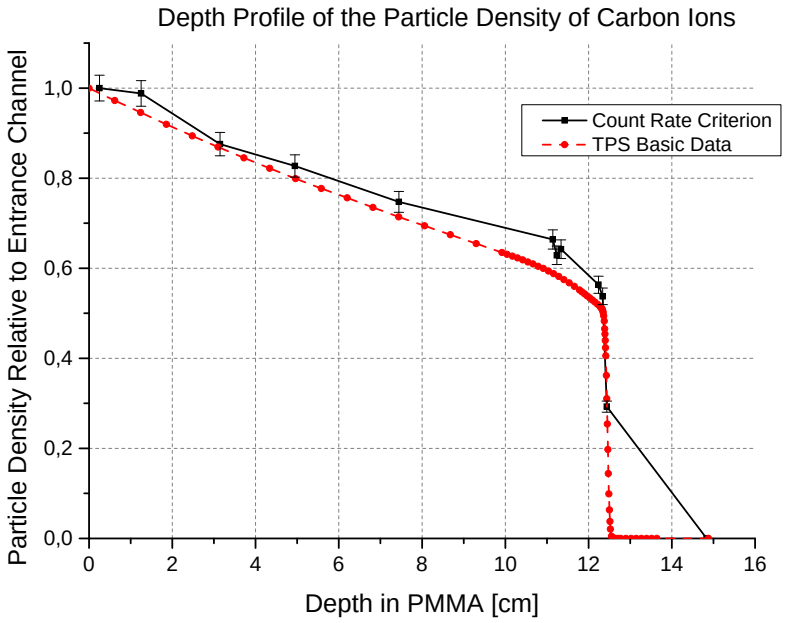

Figure 5.10.: The relative density of carbon ions is plotted as a function of depth in PMMA using the intensity criterion as well as the TPS data. The error bars represent the Poisson standard deviation.

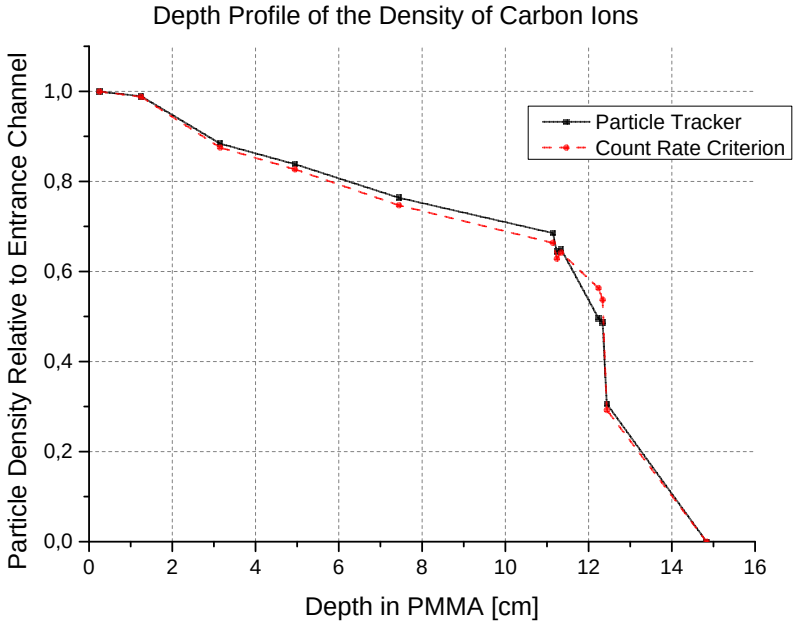

Figure 5.11.: The relative density of carbon ions is plotted as a function of depth in PMMA using the 'Particle Tracker' method and the intensity criterion.

In a next step, the mean adjusted count rate $\bar{\eta}_{adj}$, which is a proxy for LET, is plotted as a function of penetration depth. In the same plot, the dose-weighted and fluence-weighted LET of 270.55 MeV/u carbon ions using the TPS basic data is shown. LETs were calculated using the 'libamtrack' package.

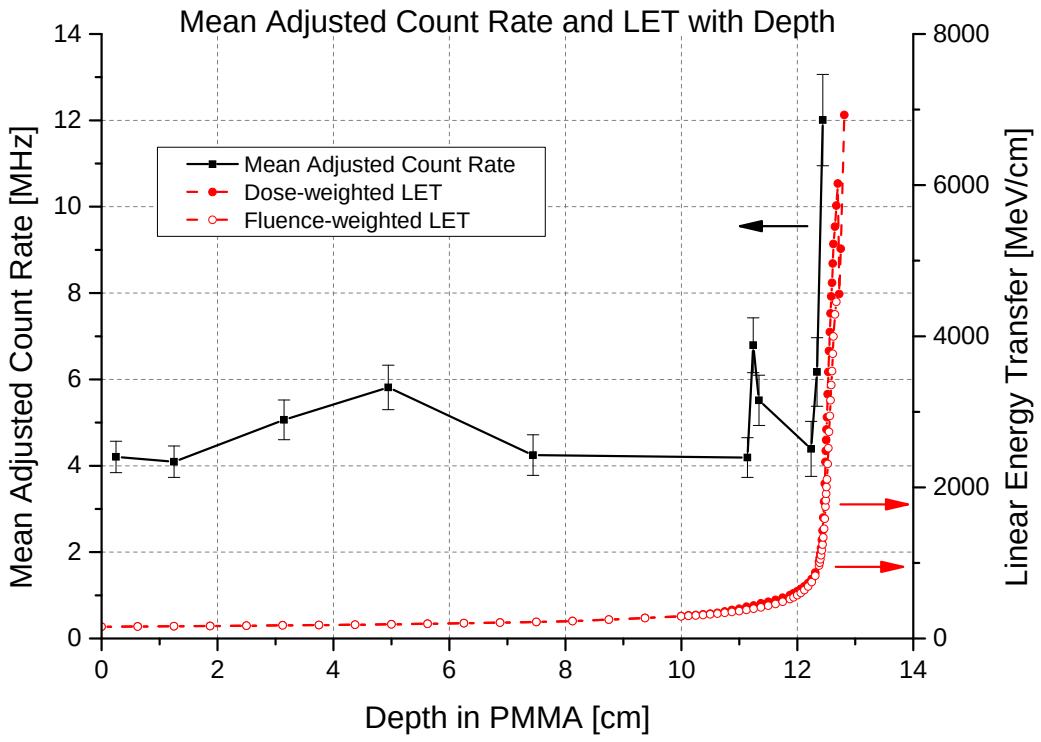

Figure 5.12.: The mean adjusted count rate $\bar{\eta}_{adj}$ for each penetration depth is shown together with the dose-weighted and fluence-weighted LET obtained from the SPC file for 270.55 MeV carbon ions. The values for the adjusted count rate in the Bragg peak are underestimated due to non-linearities, discussed in Sec. 6.2.2.

6. Discussion

6.1. Depth Profiles and Angular Discrimination of Protons

6.1.1. Depth Profile of Proton Densities using Manual Discrimination

The characteristic depth profile of particle densities with a gradual decrease in the first part and a strong falling in the Bragg peak was verified for a proton beam (Fig. 5.1). If we consider the total particle densities for penetration depths as low as 11.340 cm in PMMA, a difference of 4.5% at the maximum and an average difference of 3.3% between the simulation and this method was observed. In greater depths, the difference becomes larger. This is due to slightly different depths used in the experiments at HIT and in the simulation. Also, the value for the WEPL used for the planning of the experiments might contain a relevant error. The simulation did not take this into account compared with the SPC files for which the FLUKA data are adjusted to experimental results performed at HIT. The Poisson standard deviation explains a relevant amount of this difference in depths lower 11.340 cm (approx. 1.5%). Furthermore, the simulation was run with relatively low statistics leading to an error of 1.1% in the entrance channel up to 2.0% in a depth of 12.439 cm in PMMA.

If considering the discrimination in undeflected and deflected particles, one can see that the difference for the density of undeflected protons and the FLUKA simulation becomes smaller compared to the total particle density (Fig. 5.1). For penetration depths of 11.340 cm and lower, a correlation better than 2.1% with an average deviation of 0.8% can be observed using a deflection angle for the simulation which deviates by 2° from the experimentally determined angle. Greater penetration depths again give larger differences due to slight deviations for depths used in the experiment and the simulation. The particle densities from the simulation had errors from 1.1% to 2%. Together with the Poisson error of the experimental results (approx. 1.5%) and the slightly different deflection angles, all deviations can be explained for depths less or equal 11.340 cm in PMMA.

For the particle density of deflected protons, a clear increase towards the Bragg peak can be seen in accordance with the simulation, obtaining a maximum in the same depth within a range of 2 mm (Fig. 5.1). However, the particle density is considerably lower compared to the simulation. An explanation might be low statistics for the number of deflected protons leading to great errors for the Poisson distribution of the particle

beam. Furthermore, the manual discrimination of deflected and undeflected particles may not be very accurate. But also, the simulation gave errors for the particle density of 4% in the minimum (up to 6% for all depths, without taking the value in the entrance channel and the value far behind the Bragg peak into account).

Although this manual method provided the most accurate data for the detection of protons with depth, it is too pedestrian to examine every single particle track for a huge number of particles. The statistics collected in this thesis was still too low to make a reliable assertion with respect to a very high accuracy. Therefore, a second more convenient method was investigated which will be discussed in the following section.

6.1.2. Depth Profile of Proton Densities and Angular Discrimination using Variance and Covariance Criteria

This method used variances and covariances of particle tracks in order to discriminate between deflected and undeflected particles. The parameters were adjusted to particle tracks produced in the detector behind 12.439 cm of PMMA. For tracks produced in this FNTD, a correlation between the deflection angle of protons and the variance or covariance of the corresponding tracks was observed (Fig. 4.10 and 4.11). Tracks in the entrance channel, however, had not the same clear structure as those detected in larger depths. Therefore, it has been learned that this approach is not a robust method for such track spots.
If one compares the manual method with this one, it can be seen that the values for the manually determined particle density are always greater than the particle densities determined with the variance/covariance method (Fig. 5.3). Also, we can see that the difference between both methods decreases considerably with rising depth starting with a difference of 14.4% in the entrance channel. For depths beyond 7.443 cm, we obtain differences lower than 5%. For depths from 12.139 to 12.639 cm, the difference decreases from 4% down to 0.7% with zero percent difference within the errors obtained by the linear regression. Therefore, for tracks with widths above a certain threshold and uniform intensity distributions within the tracks, this method seems to work. However, there are still inaccuracies, which need to be corrected for a reliable use of this method, already mentioned in Sec. 4.4.2. Reasons might be:

A. Two adjacent tracks can affect the variance and covariance of each other significantly.

B. Tracks of secondary electrons attached to particle tracks can have large influences on variance and covariance of the particle track.

C. Tracks at the edge of an image are cut off and have therefore distorted variances or covariances.

Furthermore, this approach does not work above a certain value for the length of a track if only disks with small mask radii are applied. Greater mask radii, however, make issues

A and B worse and should therefore not be chosen. To make more reliable statements regarding this method, a lot more data would need to be analysed.
The manual method (Sec. 5.1.1) appeared to be the more accurate method investigated in this thesis if comparing the results with the FLUKA simulation.

6.1.3. Depth Profile of Fluorescence Intensity Signals of Protons

The results have shown that the intensity of the fluorescence signal of particle tracks increases with rising penetration depth in PMMA. As we know that the intensity is correlated to LET [5, 6], this confirms that one can see a correlation of intensity and the dose-weighted or the fluence-weighted LET with depth (Fig. 5.6).
For undeflected particles, one can observe that the intensity is lower at all penetration depths which is probably due to more elongated particle tracks. This means that the intensity signal is more spread out than for fairly round track spots.

6.2. Depth Profiles and Particle Discrimination in a Carbon Ion Beam

6.2.1. Depth Profile of Carbon Ion Densities using the 'Mosaic' Particle Tracker

It can be seen that the results are consistent with the ground truth (SPC file). However, the experimentally obtained particle densities for carbon ions are systematically above the simulated carbon ion densities which cannot be explained with the Poisson distribution in the particle beam only (Fig. 5.7). Furthermore, an increasing difference with rising depth between these results and the SPC file can be observed for penetration depths as low as 11.340 cm. A reason for these observations might be that tracks produced by fragments, such as lithium, beryllium and boron, were considered to be produced by carbon ions since they cannot be discriminated by eye due to very similar shape and intensity. Furthermore, the Poisson error for the particle densities varied from 2.0% to 2.9% in front of the Bragg peak. These reasons could explain the deviation from the SPC file.

6.2.2. Depth Profile of Carbon Ion Densities using Track Intensity Signals and Depth Profile of Track Intensities

The results for the particle density of carbon ions are in consistence with the SPC file and furthermore, show smaller deviations than the method using the particle tracker involving the visually determined threshold (Fig. 5.10 and 5.11). However, the particle densities are still systematically above those of the SPC file. Nevertheless, it is likely that this method detects less heavy fragments such as lithium, beryllium or boron. An average deviation of 6.8% from TPS data for depths lower 12.4 cm was obtained.

In Fig. 6.1, the histogram of the adjusted count rates for particles detected in the FNTD lb1011 is shown. The approximate positions for the intensity of fragments are indicated. This gives rise to assume that at least all boron fragments were taken into account for the detection of carbon ions which would explain most deviations from the SPC file together with the Poisson error (approx. 2.4%), as seen in Fig. 6.2. If taking boron ions into account, the particle density of carbon ions decreases to an average deviation of 1.9%.

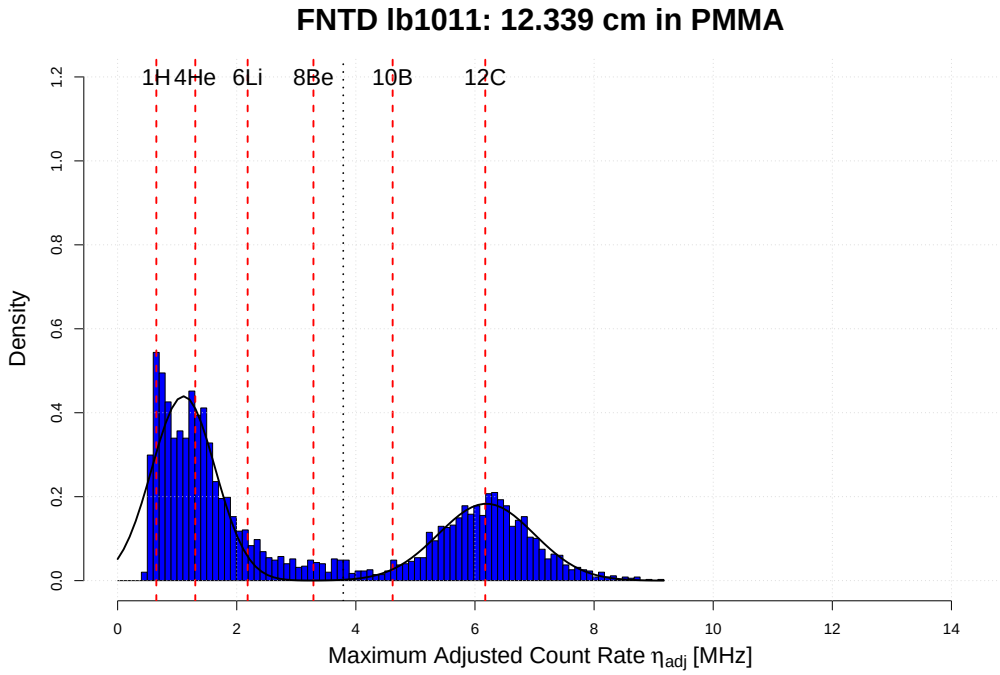

Figure 6.1.: Histogram of the adjusted count rate for FNTD lb1011. The dashed lines represent the approximate positions for fragments in a carbon ion beam. The dotted line indicates the 3σ range on the left-hand side of the ^{12}C peak. All values greater than this limit were considered to be carbon ions.

Concerning the histograms of the fluorescence signal of particle tracks (Fig. 5.8 and 5.9), two peaks can be seen with their width getting larger with depth. The left peak increases in the number of count rates with depth while the right peak decreases. The left peak was therefore assumed to indicate proton fragments, but the tail on the right-hand side of this peak was observed to get larger with depth. In depths greater than 12.3 cm, one can assume a second peak for a slightly greater adjusted count rate. This peak could indicate helium fragments, being the second most frequent fragments in a carbon ion beam. The assumption of a double Gaussian fit would then not be correct for this intensity distribution. Also, we can observe a right shift of the carbon ion peak in greater penetration depths whereas the proton (and helium) peak does not increase in the count rate on the same level in accordance with the LET of carbon ions and fragments.

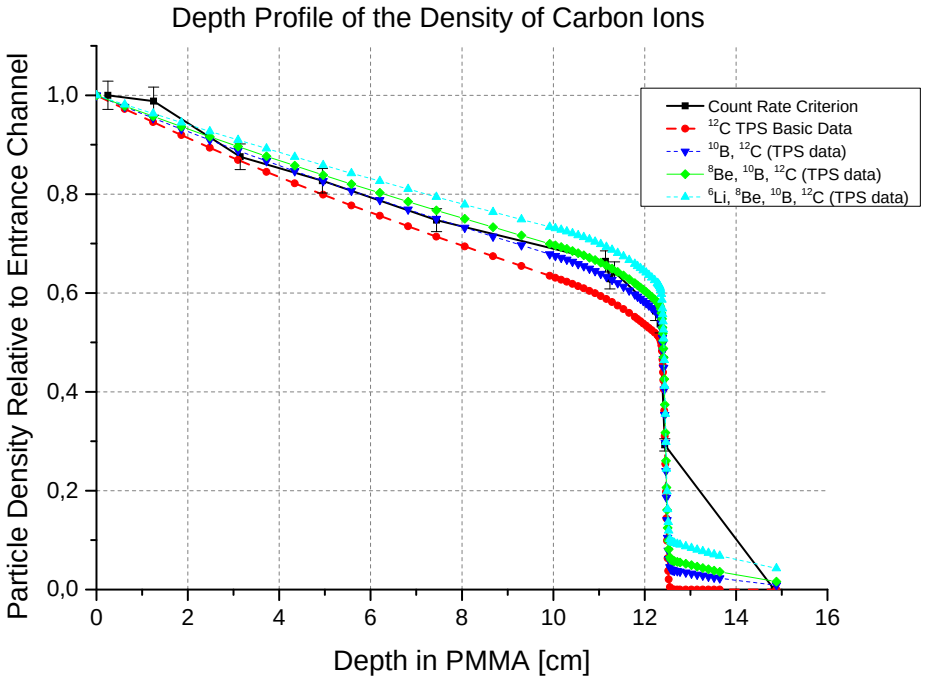

Figure 6.2.: The relative density of carbon ions is plotted as a function of depth in PMMA. The error bars represent the Poisson standard deviation. The relative densities of carbon ions, including different types of fragments, taken from the TPS basic data, are also shown.

Regarding the plot which shows the mean adjusted count rate with depth (Fig. 5.12), the count rate increases rapidly in the Bragg peak just as LET, illustrating the correlation of the intensity signal and LET with depth. The maximum value for the mean adjusted count rate is 12 MHz and does not correspond, due to non-linearities, to the actual count rate, which is assumed to be linear with laser power. The corresponding actual count rate is even higher (approx. 22 MHz) whereas for count rates around 4 MHz the expected count rate is roughly 4.6 MHz using calculations from [20] for the average saturation count rate.
In front of the Bragg peak, we expected to see the same behaviour as for LET, i.e. a smooth increase of intensity with depth. For some values for the count rate, however, one can see clear deviations from this behaviour. One reason might be that different microscope settings compared to images of the other detectors were chosen by mistake. Doing the read-out process again would clarify this issue, but for time reasons it was not possible to do this. Another explanation might be that the concentration of colour centres varies within the crystal, which can lead to more or to less colour centres converted, resulting in a higher or lower intensity signal. However, this is not expected to explain the entire deviation.

7. Conclusion and Outlook

Current research projects focus on the investigation of the suitability of FNTDs for in-vivo usage in clinical applications. In a first step, in-vivo ion range measurements have shown promising results for clinical use [7]. As a next step, the applicability of FNTDs for the detection of heavy charged particles with depth was investigated in this thesis. It was shown that FNTDs are suitable for the detection of protons and carbon ions with increasing penetration depth in PMMA. For protons, an average deviation from FLUKA simulations of 3.3% with a maximum difference of 4.5% was obtained for depths lower 11.5 cm. For a carbon ion beam, the particle density was determined with less accuracy since boron fragments were very likely considered to be carbon ions. An average deviation of 6.8% from TPS data for depths lower 12.4 cm was obtained. Taking boron ions into account decreases the average deviation to 1.9%.

Further studies focussed on the investigation of two methods for the determination of deflection angles of particles in order to find a convenient method for the determination of fluences with depth. However, the most accurate method still includes the acquisition of stacks of images in different depths within the FNTD crystal. This allows for a very accurate determination of deflection angles of particles penetrating an FNTD.
The method utilizing variances or covariances of particle tracks has shown that these measures are linearly correlated to the deflection angles of particles. However, this method works only for tracks with large widths and clear intensity distributions. If only a single image of an FNTD is available, this method can be at least used as a makeshift solution.
A further investigation focussed on incipient stages concerning discrimination of different particle types in a carbon ion beam. The detection of carbon ions with increasing depth has shown that it is possible to discriminate between lighter fragments, such as protons and helium, and carbon ions. For heavier fragments, a reliable discrimination was not possible in this thesis, but a more detailed analysis should show clear distinguishing features for those particle types due to a lower intensity of fragments and smaller track widths. Maximum intensity projections might be a solution since deflection angles were relatively low for heavy particles.

The fluorescence intensity signal of particle tracks, which is a proxy for LET, was investigated with depth for both a proton and a carbon ion beam. It has shown the characteristic behaviour for LET with a rapid increase approximately in the Bragg Peak for protons. A strong rise in the Bragg peak was also shown for a carbon ion beam, but a stronger varying signal in lower depths was found. Therefore, further investigations for an accurate determination of LET in depth need to be done.

The FNTDs irradiated in experiments for this thesis are currently read out using stacks of images with depth within the crystal. The angular distribution of particles can be assessed and additionally, high statistics should allow for a very accurate determination of fluences in different penetration depths using these stacks. An advantage of carbon ions over protons with respect to fluence determinations might be lower deflection angles, since carbon ion tracks can therefore more easily be detected with depth within the FNTD using the current detection techniques. Furthermore, in a next step angular irradiations in different depths can be read out and analysed using stacks of images.

Further evaluations regarding the detection and discrimination of carbon ions and fragments can be done. The intensity criterion for the particle track detection can be used for a larger number of particles obtaining a greater number of heavy fragments which can be analysed. Since the quantitative correlation of intensity and LET is known with an uncertainty of 14% [6], all particle types in a carbon ion beam should be differentiated utilising FNTDs. Moreover, current investigations on the normalisation of intensity signals may reduce this uncertainty.

Appendices

A. Abbreviations

Al_2O_3:C,Mg	Aluminium oxide doped with carbon and magnesium
APD	Avalanche Photodiode
DKFZ	Deutsches Krebsforschungszentrum (German Cancer Research Center)
F-centre	Colour centre
FLUKA	FLUktuierende KAskade
FNTD	Fluorescent Nuclear Track Detector
HCP	Heavy charged particle
HIT	Heidelberg Ion-Beam Therapy Center
LET	Linear Energy Transfer
LSM	Laser Scanning Microscope
MC	Monte Carlo (simulation)
NIR	Near-infrared
PMMA	Poly(methyl methacrylate) or acrylic glass
SNR	Signal-to-noise ratio
WEPL	Water equivalent path length

B. LSM 710 Settings for Image Acquisition and Image Positions

The settings used for image acquisition of all FNTDs analysed in this thesis are shown in Tab. B.1. The exact positions within the detector are listed in Tab. B.2 and B.3. The zero point was set to the position seen in Fig. B.1.

Laser type	HeNe laser (633 nm)
Relative laser power p	100%
Dwell time τ	68.92 µs
Pinhole diameter d_p	1 AU
Image size in μm^2	168.69
Image size in px^2	1500
Zoom	0.8
Digital gain g	0.2
Digital offset Δg	0
Bit depth	16 bit
Rescans R (lb1000 series)	8
Rescans R (lb2000 series)	4
Rescans R (all z-stacks)	1

Table B.1.: LSM 710 settings for image acquisition.

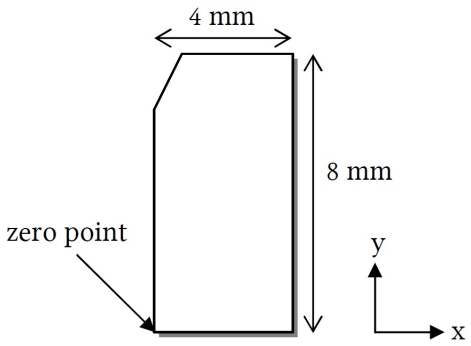

Figure B.1.: Sketch of an FNTD showing the definition of the zero point for image positioning. The zero point was set to the bottom left corner of the FNTD aligned to the bottom left edge of the scan display in the ZEN software.

FNTD ID	X [mm]	Y [mm]	Z [µm]
lb1000	1.815	4.079	25
	1.990	3.789	25
	2.122	3.968	25
lb1001	2.008	4.116	25
	2.161	3.866	25
	1.735	3.866	25
lb1002	2.287	3.897	25
	2.287	4.124	25
	1.941	4.116	25
lb1003	2.113	4.027	25
	1.916	4.027	25
	1.851	4.199	25
lb1004	1.819	4.095	25
	2.017	4.095	25
	1.729	4.295	25
lb1005	1.844	4.162	25
	1.991	3.970	25
	2.216	4.155	25
lb1006	1.926	3.836	25
	1.970	4.150	25
	2.193	3.995	25
lb1007	2.456	4.085	25
	2.152	4.085	25
	2.245	3.881	25
lb1008	2.072	4.165	25
	2.290	4.199	25
	2.283	3.949	25
lb1008 z-stack	1.941	3.467	0 to 100 à 1
lb1009	1.880	3.883	25
	1.880	4.089	25
	2.340	4.006	25
lb1010	2.101	3.887	25
	2.196	4.157	25
	1.845	4.157	25
lb1011	1.805	3.948	25
	2.033	3.948	25
	1.911	4.152	25
lb1011 z-stack	2.048	3.929	0 to 100 à 1

Table B.2.: Image positions for FNTDs irradiated with carbon ions.

FNTD ID	X [mm]	Y [mm]	Z [µm]
lb2000	1.797	4.069	25
	2.201	4.069	25
	2.276	3.838	25
	1.829	3.838	25
lb2001	1.615	4.273	25
	1.838	4.273	25
	1.520	4.012	25
	1.776	4.012	25
lb2002	1.687	4.150	25
	1.895	4.150	25
	1.895	3.776	25
	1.738	3.535	25
lb2003	2.281	4.237	25
	2.022	4.211	25
	2.054	4.063	25
	2.534	4.063	25
lb2004	1.805	3.971	25
	2.047	3.979	25
	2.061	4.290	25
	1.688	4.290	25
lb2005	1.187	3.228	25
	1.409	3.289	25
	1.350	3.517	25
	1.146	3.555	25
lb2006	1.860	3.922	25
	2.056	3.922	25
	2.056	4.142	25
	1.849	4.142	25
lb2007	1.816	4.095	25
	2.041	4.095	25
	2.041	3.895	25
	1.845	3.895	25
lb1007 z-stack	2.218	4.011	0 to 100 à 1
lb2008	1.611	4.163	25
	1.841	4.163	25
	1.664	3.940	25
	1.911	4.014	25
lb2009	1.671	3.785	25
	1.890	3.785	25
	1.806	4.033	25
	1.601	4.147	25

Table B.3.: Image positions for FNTDs irradiated with protons.

C. Detection of Carbon Ion Tracks using the Particle Tracker

The detection of carbon ion tracks using the 'Mosaic' particle tracker was tried to be automated in order to find a suitable percentile parameter. For a defined range of values with a small step size, the number of detected tracks was determined automatically. Fig. C.1 and C.2 show the number of detected tracks as a function of percentile for all penetration depths. One can see that this method works as long as the detector is placed into the entrance channel giving a plateau for a range of percentile parameters. In greater depths, the plateau gets smaller due to the detection of tracks produced by fragments or due to multiple detected elongated tracks. However, the plots might give a little hint for discriminating between tracks of carbon ions and of such produced by fragments.

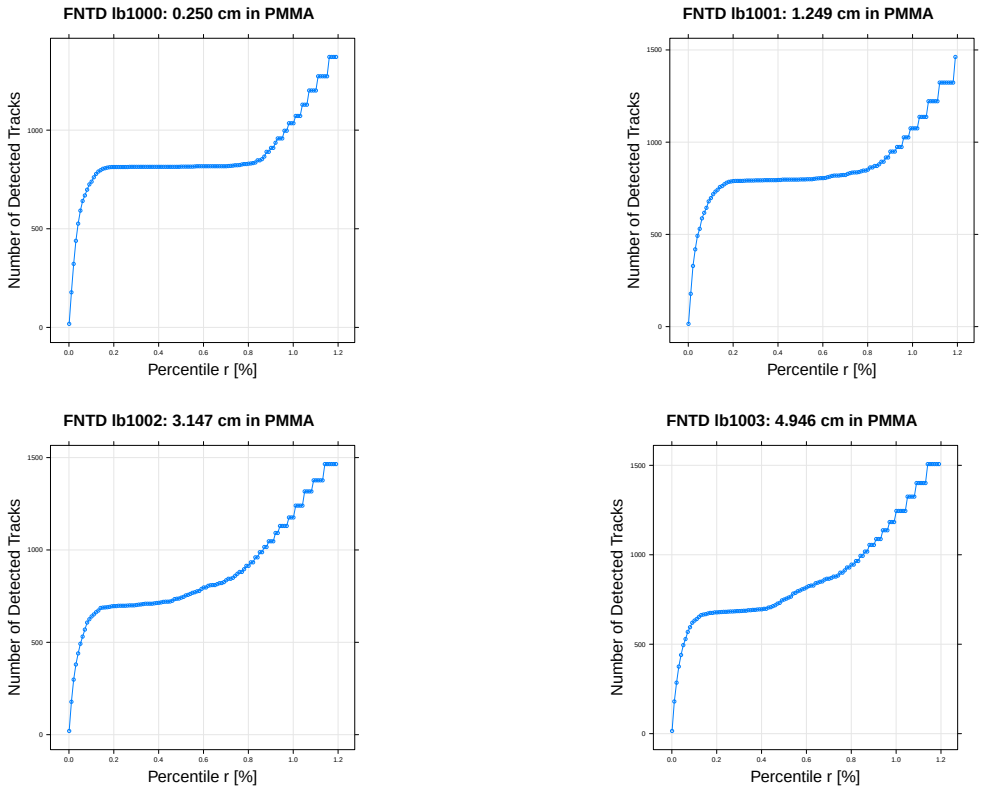

Figure C.1.: The number of detected tracks is plotted as a function of the percentile parameter for a single image of FNTDs lb1000 to lb1003.

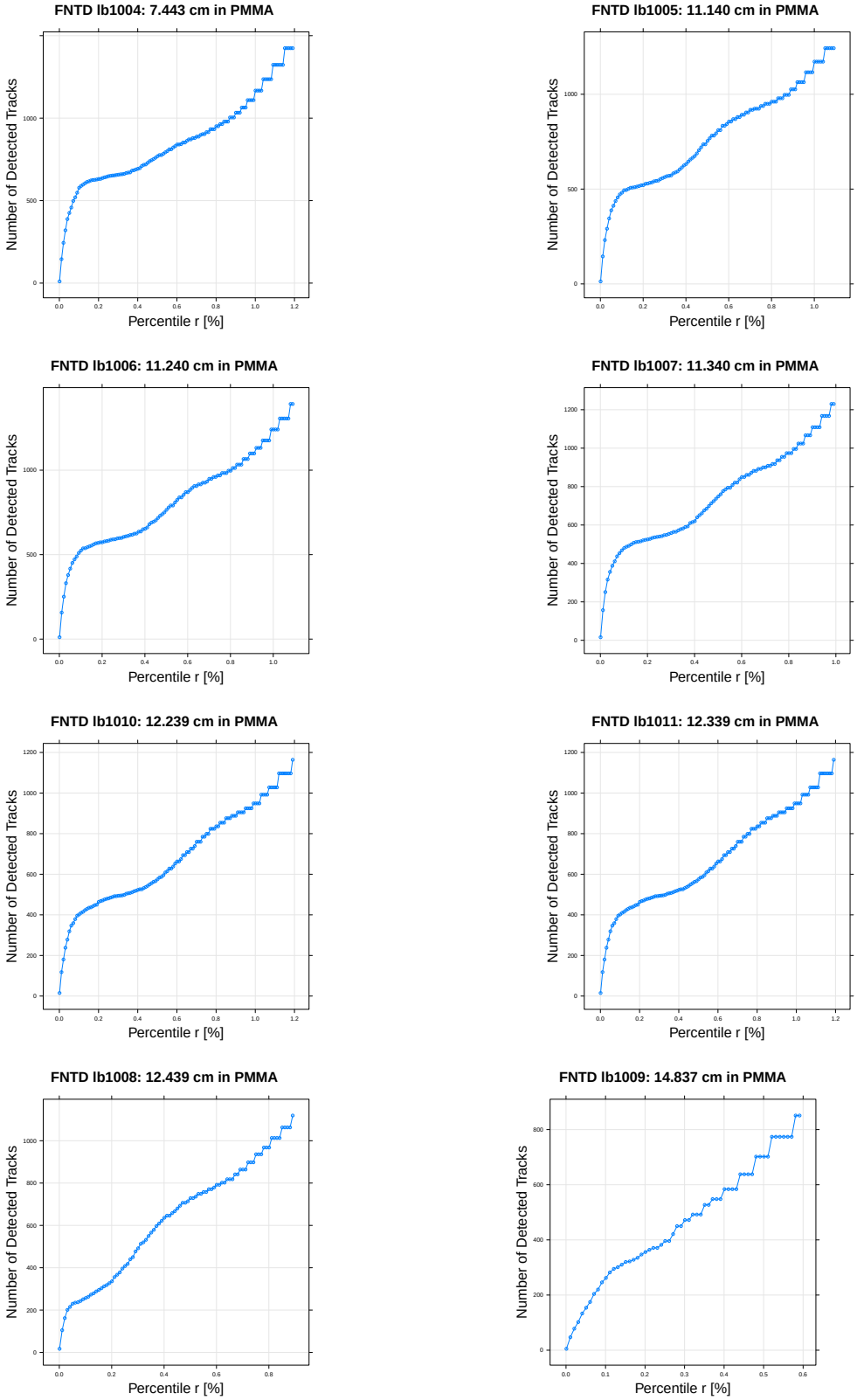

Figure C.2.: The number of detected tracks is plotted as a function of the percentile parameter for a single image of FNTDs lb1004 to lb1011.

List of Figures

List of Tables

Bibliography

[1] Schulz-Ertner, D. & Tsujii, H. Particle radiation therapy using proton and heavier ion beams. *Journal of Clinical Oncology* **25**, 953–964 (2007). URL http://jco.ascopubs.org/content/25/8/953.abstract. http://jco.ascopubs.org/content/25/8/953.full.pdf+html.

[2] Schardt, D., Elsässer, T. & Schulz-Ertner, D. Heavy-ion tumor therapy: Physical and radiobiological benefits. *Rev. Mod. Phys.* **82**, 383–425 (2010). URL http://link.aps.org/doi/10.1103/RevModPhys.82.383.

[3] Karger, C. P. & Jäkel, O. Current status and new developments in ion therapy. *Strahlentherapie und Onkologie* **183**, 295–300 (2007). URL http://www.ncbi.nlm.nih.gov/pubmed/17520182.

[4] Osinga, J.-M. *et al.* High-Accuracy Fluence Determination in Ion Beams using Fluorescent Nuclear Track Detectors. *Radiation Measurements* **in press** (2013). URL http://www.sciencedirect.com/science/article/pii/S1350448713000589.

[5] Sykora, G. J., Akselrod, M. S., Benton, E. & Yasuda, N. Spectroscopic properties of novel fluorescent nuclear track detectors for high and low LET charged particles. *Radiation Measurements* **43**, 422–426 (2008). URL http://linkinghub.elsevier.com/retrieve/pii/S135044870700457X.

[6] Niklas, M. *et al.* Spatial correlation between traversal and cellular response in ion radiotherapy - towards single track spectroscopy. *Radiation Measurements* (2013). URL http://linkinghub.elsevier.com/retrieve/pii/S1350448713000838.

[7] Klimpki, G. *et al.* Ion Range Measurements using Fluorescent Nuclear Track Detectors. *Radiation Measurements* (2013). URL http://linkinghub.elsevier.com/retrieve/pii/S1350448713001467.

[8] Krieger, H. *Grundlagen der Strahlungsphysik und des Strahlenschutzes*. SpringerLink : Bücher (Vieweg+Teubner Verlag, Wiesbaden, 2012), 4. aufl. 2012. überarb. u. erw edn. URL http://dx.doi.org/10.1007/978-3-8348-2238-3;http://dx.doi.org/10.1007/978-3-8348-2238-3.

[9] Icru report 85. *Journal of the ICRU* **11**, NP (2011). URL http://jicru.oxfordjournals.org/content/11/1/NP.2.short.

[10] Kraft, G., Krämer, M. & Scholz, M. Let, track structure and models. *Radiation and Environmental Biophysics* **31**, 161–180 (1992). URL http://dx.doi.org/10.1007/BF01214825.

[11] Kase, K. R. H. (ed.) *The dosimetry of ionizing radiation* (Acad. Pr., Orlando [u.a.]).

[12] Krieger, H. *Strahlungsmessung und Dosimetrie.* SpringerLink : Bücher (Springer Spektrum, Wiesbaden, 2013), 2., überarb. u. erw. aufl. 2013 edn. URL http://dx.doi.org/10.1007/978-3-658-00386-9;http://dx.doi.org/10.1007/978-3-658-00386-9.

[13] Osinga, J. M. *Fluorescent Nuclear Track Detectors: High-Accuracy Fluence Determination in Ion Beams.* Master's thesis, Martin Luther University of Halle-Wittenberg, Germany (2012).

[14] Akselrod, M. S. & Orlov, S. S. One-bit recording and fluorescent confical readout utilizing aluminum oxide signle crystals. *Optical Data Storage* **5069**, 252–256 (2003).

[15] Akselrod, G. M., Akselrod, M. S., Benton, E. & Yasuda, N. A novel Al2O3 fluorescent nuclear track detector for heavy charged particles and neutrons. *Nuclear Instruments and Methods in Physics Research Section B: Beam Interactions with Materials and Atoms* **247**, 295–306 (2006). URL http://linkinghub.elsevier.com/retrieve/pii/S0168583X06001315.

[16] Akselrod, M. S., Akselrod, A. E., Orlov, S. S., Sanyal, S. & Underwood, T. H. Fluorescent Aluminum Oxide Crystals for Volumetric Optical Data Storage and Imaging Applications. *Journal of Fluorescence* **13**, 503–511 (2003). URL http://www.springerlink.com/openurl.asp?id=doi:10.1023/B:JOFL.0000008061.71099.55.

[17] Akselrod, M. S., Akselrod, A. E., Orlov, S. S., Sanyal, S. & Underwood, T. H. New aluminum oxide single crystals for volumetric optical data storage. *Optical Data Storage* **5069**, 244–250 (2003).

[18] Combs, S. E., Jäkel, O., Haberer, T. & Debus, J. Particle therapy at the heidelberg ion therapy center (hit) integrated research-driven university-hospital-based radiation oncology service in heidelberg, germany. *Radiotherapy and Oncology* **95**, 41 – 44 (2010). URL http://www.sciencedirect.com/science/article/pii/S016781401000109X.

[19] Heidelberg ion-beam therapy center (2013). URL http://www.klinikum.uni-heidelberg.de/Heidelberger-Ionenstrahl-Therapie-HIT.112189.0.html.

[20] Greilich, S. *et al.* Fluorescent Nuclear Track Detectors as a Tool for Ion-Beam Therapy Research. *Radiation Measurements* **in press** (2013). URL http://www.sciencedirect.com/science/article/pii/S1350448713000565.

[21] Rasband, W. S. *ImageJ.* U.S. National Insitutes of Health, Bethesda, Maryland, USA, URL: http://rsb.info.nih.gov/ij/ (2013) .

[22] Team, R. D. C. *R: A language and environment for statistical computing.* (R Foundation for Statistical Computing, Vienna, Austria, 2013). URL ISBN3-900051-07-0.

[23] Sbalzarini, I. F. & Koumoutsakos, P. Feature point tracking and trajectory analysis for video imaging in cell biology. *Journal of structural biology* **151**, 182–95 (2005). URL http://www.ncbi.nlm.nih.gov/pubmed/16043363.

[24] Hoof, S. *Correlation of Particle and Background Signal in Al_2O_3:C,Mg Fluorescent Nuclear Track Detectors.* Bachelor's thesis, Ruprecht-Karls-University Heidelberg, Germany (2013).

[25] Battistoni, G. *et al.* The fluka code: description and benchmarking. *AIP Conference Proceedings* **896**, 31–49 (2007). URL http://link.aip.org/link/?APC/896/31/1.

[26] Ferrari, A., Sala, P. R., Fasso, A. & Ranft, J. FLUKA: A multi-particle transport code (Program version 2005) (2005).

[27] Greilich, S. & the libamtrack team. Libamtrack package. (2013). URL https://libamtrack.dkfz.de/.

[28] Klimpki, G. M. *Towards in-vivo ion range measurements using fluroescent nuclear track detectors.* Bachelor's thesis, Ruprecht-Karls-University Heidelberg, Germany (2012).

[29] Martel, R. *Werkzeuge zur Untersuchung des Hintergrundes von fluoreszierenden Kernspurdetektoren.* Bachelor's thesis, Ruprecht-Karls-University Heidelberg, Germany (2012).

Acknowledgements

I am truly grateful for the support I achieved during the time I carried out this thesis. Especially, I would like to thank Prof. Dr. Schlegel for accepting me in the Division of Medical Physics in Radiation Oncology at the DKFZ and Prof. Dr. Jäkel who admitted me in his research group and for being my supervisor and second referee. Also, I would like to thank Prof. Dr. Bachert for being my first referee and being the representative of the Department of Physics and Astronomy.

My special thanks go to Dr. Steffen Greilich. During my time at the DKFZ, I learned so many things from him. He supported me with so many ideas and always motivated me to try out this or that. Without him, this thesis would not have been possible. Also, I would like to thank Julia-Maria Osinga. She supported and helped me a lot during my work, especially for the planning and the irradiation at HIT. I would like to thank Martin Niklas for advice and assistance regarding the evaluation of my data. Furthermore, I have to thank all the people from the Heavy Ion Therapy group and in particular, all the people from the FNTD meeting: Sebastian Hoof, Thomas Rösch and Nicolas Schudell.

I would like to thank the staff from HIT for giving me sufficient beam time for my experiments, especially Dr. Stefan Brons for many important advices and helpful support for the planning and the irradiations at HIT. Furthermore, I have to thank Dr. Felix Bestvater, Damir Krunic and all the people from the Light Microscope Facility at the DKFZ for giving me an introduction how to operate the microscope and providing enough read-out time. Moreover, I would like to thank Armin Runz and all the people from the manufacture for producing the PMMA equipment used in experiments for this thesis.

Declaration

Ich versichere, dass ich diese Arbeit selbstständig verfasst und keine anderen als die angegebenen Quellen und Hilfsmittel benutzt habe.
Heidelberg, den